

Evaluation of Riemann flux solvers for WENO reconstruction schemes: Kelvin–Helmholtz instability



Omer San ^{a,*}, Kursat Kara ^b

^aInterdisciplinary Center for Applied Mathematics, Virginia Tech, Blacksburg, VA, USA

^bDepartment of Aerospace Engineering, Khalifa University, Abu Dhabi, United Arab Emirates

ARTICLE INFO

Article history:

Received 22 April 2014

Received in revised form 17 April 2015

Accepted 30 April 2015

Available online 14 May 2015

ABSTRACT

Accurate and computationally efficient simulations of Euler equations are of paramount importance in both fundamental research and engineering applications. In this study, our main objective is to investigate the efficacy and accuracy of several Riemann solvers for high-order accurate weighted essentially non-oscillatory (WENO) reconstruction scheme as a state-of-the-art tool to study shear driven turbulence flows. The Kelvin–Helmholtz instability occurs when a perturbation is introduced to a continuous fluid system with a velocity shear, or where there is a velocity difference across the interface between two fluids. Here, we solve a stratified Kelvin–Helmholtz instability problem to demonstrate the performance of six different Riemann solvers' ability to evolve a linear perturbation into a transition to nonlinear hydrodynamic two-dimensional turbulence. A single mode perturbation is used for our evaluations. Time evolution process shows that the vortices formed from the turbulence slowly merge together since both energy and enstrophy are simultaneously conserved in two-dimensional turbulence. Third-, fifth- and seventh-order WENO reconstruction schemes are investigated along with the Roe, Rusanov, HLL, FORCE, AUSM, and Marquina Riemann flux solvers at the cell interfaces resulting in 18 joint flow solvers. Based on the numerical assessments of these solvers on various grid resolutions, it is found that the dissipative character of the Riemann solver has significant effect on eddy resolving properties and turbulence statistics. We further show that the order of the reconstruction scheme becomes increasingly important for coarsening the mesh. We illustrate that higher-order schemes become more effective in terms of the tradeoff between the accuracy and efficiency. We also demonstrate that AUSM solver provides the least amount of numerical dissipation, yet resulting in a pile-up phenomenon in energy spectra for underresolved simulations. However, results obtained by the Roe solver agree well with the theoretical energy spectrum scaling providing a marginal dissipation without showing any pile-up at a cost of around 30% increase in computational time.

© 2015 Elsevier Ltd. All rights reserved.

1. Introduction

Accurate and efficient solutions of Euler equations have been subject to intensive research for at least five decades and many successful numerical methods have been proposed for solving them (e.g., see [1–12]). Euler equations are a system of non-linear hyperbolic conservation laws that govern the dynamics of compressible material such as gases or liquids at high pressures, for which the effects of body forces, viscous stresses and heat flux are neglected [13]. They are very important for many areas including astrophysics, weather and aerospace simulations. Astrophysical gas flows are often highly supersonic and require

correct treatment of shocks and other discontinuities (e.g., contact discontinuities, across which the density and temperature jump but the pressure, and tangential discontinuities, across which the tangential velocity changes) [14]. For aeronautical applications, accurate computations of shock and vortex dominated flows are important for aerodynamics shape optimization and load calculations during conceptual and preliminary design phases [15,16].

Traditionally, second-order accurate numerical methods are often preferred in solutions of Euler equations because of their simplicity and robustness. The main deficiency of these methods for accurate computation of vortex dominated flows is the numerical diffusion of vorticity to unacceptable levels [17]. Application of high-order methods can significantly alleviate this deficiency and be more efficient for the problems requiring high accuracy, such as wave propagation problems, vortex-dominated flows, large

* Corresponding author.

E-mail address: omersan@vt.edu (O. San).

eddy simulations and direct numerical simulations of turbulence. Analysis of resolution, stability, dispersion relation preservation properties of space-time discretization schemes is an important aspect in ensuring their appropriate applications [18–20]. According to a survey done by American Institute of Aeronautics and Astronautics (AIAA) Computational Fluid Dynamics Algorithm Discussion Group (CFDADG), high-order methods typically have at least third-order spatial accuracy [21]. For review of high-order accurate methods, see [17,21–24]. A comprehensive framework on high accuracy computing methods for fluid flows and wave phenomena can be also found in a recent book [25].

After years of research on the methods to solve Euler equations accurately and efficiently, now we have many choices available to code developers or more importantly to users. Developers mostly implement all the available methods to their code. On the other hand, an inexperienced user with a flow problem to be solved will feel helpless between too many choices at each stage. To analyze the performance of these methods, several comparative studies have been performed on various range of problems targeted for different purposes [26–36], which can be considered as user guides for future problems. However, these studies are invaluable for understanding the behavior of various numerical methods for hyperbolic conservation laws, further studies are required for a better understanding to characterize certain features for complicated flows such as dissipative behavior of the methods in large eddy simulations [26,31,37–39].

One of the most successful state-of-the-art approaches for solving conservation laws is weighted essentially non-oscillatory (WENO) scheme in which an adaptive stencil that adjusts to the smoothness of the solutions is applied [40–47]. WENO schemes can be classified as reconstruction or flux-splitting based approaches. In the first approach, reconstructed left and right states are determined at the cell boundaries using WENO interpolation procedures, then a Riemann solver is usually used to calculate fluxes through these cell boundaries. Second approach requires a flux-splitting procedure, depending on the direction in which the information is propagating, to obtain positive and negative fluxes at the cell centers, and then WENO interpolation procedure can be used to compute both fluxes at the cell boundaries. In this paper, we will employ a high order accurate WENO interpolation procedure at three different orders (3rd, 5th, and 7th) to determine reconstructed left and right states at the cell edges. In this framework, to evaluate the averaged flux at cell edges, six approximate Riemann solvers are implemented including Rusanov scheme, Roe scheme, Harten, Lax and van Leer (HLL) scheme, first-order central (FORCE) scheme, advection upstream splitting method (AUSM), and Marquina scheme.

The main contribution in this study is to examine the performance of Riemann solvers for WENO reconstruction solvers. A particular emphasis is placed on characterizing the dissipative behaviors of joint solvers and their effects on turbulent flow field generated by the Kelvin–Helmholtz instability. We solve the Kelvin–Helmholtz instability problem on a two-dimensional Cartesian grid at three different grid resolutions (256^2 , 512^2 and 1024^2) using periodic boundary conditions. This problem yields a viable computational framework for studying two-dimensional hydrodynamic turbulence which is profoundly different from three-dimensional turbulence due to different energy cascade behavior, and follows the Kraichnan–Batchelor–Leith (KBL) theory [48–50]. The physics of two-dimensional turbulence has been elucidated substantially during the past decades by theoretical models, intensive numerical investigations, and dedicated soap film experiments (e.g., see [51–55]).

In the present study, six different Riemann solver were combined with WENO reconstruction scheme at three different order

of accuracy. The results obtained by these joint solvers show that the choice of Riemann solver has a significant effect on eddy resolving properties as well as turbulent statistics. We show that the predicted energy spectrum asymptotically converged to the theoretical k^{-3} scaling as the resolution increased, which is predicted by the KBL theory for forward cascading two-dimensional turbulence. Although most of the studies on two-dimensional turbulence are being conducted on solving incompressible flow equations, our results can be also considered as numerical confirmations to KBL theory for compressible flows.

The paper is organized as follows. The governing equations for inviscid compressible flows are briefly introduced in Section 2. The numerical methods are presented in Section 3 by using a modular approach with joint WENO reconstruction schemes and approximate Riemann solvers. The results for these joint schemes and solvers are presented in Section 4 for solving two-dimensional turbulence triggered by the Kelvin–Helmholtz instability. Finally, the conclusions and some comments on the performance of these numerical methods are summarized in Section 5.

2. Mathematical model

The considered governing equations in this work are the two-dimensional Euler equations written in conservative form:

$$\frac{\partial q}{\partial t} + \frac{\partial F}{\partial x} + \frac{\partial G}{\partial y} = 0 \quad (1)$$

where

$$q = \begin{pmatrix} \rho \\ \rho u \\ \rho v \\ \rho e \end{pmatrix}, \quad F = \begin{pmatrix} \rho u \\ \rho u^2 + p \\ \rho uv \\ \rho uH \end{pmatrix}, \quad G = \begin{pmatrix} \rho v \\ \rho uv \\ \rho v^2 + p \\ \rho vH \end{pmatrix}$$

in which

$$H = e + p/\rho, \quad p = \rho(\gamma - 1)\left(e - \frac{1}{2}(u^2 + v^2)\right). \quad (2)$$

Here, ρ and p are respectively the density and pressure; u and v are horizontal and vertical components of the velocity; e and H denote the internal energy and static enthalpy; γ is the ratio of specific heats. In two-dimensional Euler equations, the convective flux Jacobian matrices, $A = \frac{\partial F}{\partial q}$ and $B = \frac{\partial G}{\partial q}$, can be derived as

$$A = \begin{pmatrix} 0 & 1 & 0 & 0 \\ \phi^2 - u^2 & (3 - \gamma)u & -(\gamma - 1)v & \gamma - 1 \\ -uv & v & u & 0 \\ (\phi^2 - H)u & H - (\gamma - 1)u^2 & -(\gamma - 1)uv & \gamma u \end{pmatrix}$$

$$B = \begin{pmatrix} 0 & 0 & 1 & 0 \\ -uv & v & u & 0 \\ \phi^2 - v^2 & -(\gamma - 1)u & (3 - \gamma)v & \gamma - 1 \\ (\phi^2 - H)v & -(\gamma - 1)uv & H - (\gamma - 1)v^2 & \gamma v \end{pmatrix}$$

where $\phi^2 = \frac{1}{2}(\gamma - 1)(u^2 + v^2)$. Because Euler system is hyperbolic, there exists a similarity transform

$$LAR = A \Rightarrow A = RAL$$

$$SBT = \Psi \Rightarrow B = T\Psi S$$

where A and Ψ are respectively the diagonal matrices of the real eigenvalues of A and B ; R and T are the right eigenvector matrices, the columns of which are the right eigenvectors of A and

$B; L = R^{-1}$ and $S = T^{-1}$ are the left eigenvector matrices, the rows of which are the left eigenvectors of A and B . The eigenvalue matrices Λ and Ψ are uniquely defined in the system

$$\Lambda = \begin{pmatrix} u & 0 & 0 & 0 \\ 0 & u & 0 & 0 \\ 0 & 0 & u+a & 0 \\ 0 & 0 & 0 & u-a \end{pmatrix}, \quad \Psi = \begin{pmatrix} v & 0 & 0 & 0 \\ 0 & v & 0 & 0 \\ 0 & 0 & v+a & 0 \\ 0 & 0 & 0 & v-a \end{pmatrix}$$

where a is the speed of the sound and defined as $a^2 = \gamma p/\rho$. The eigenvector matrices are defined in [36].

3. Numerical methods

In this section, we briefly describe the numerical schemes used in our computations. The semi-discrete form of the Euler equations given in Eq. (1) can be written as

$$\frac{dq_{ij}}{dt} + \frac{1}{\Delta x} (F_{i+1/2,j} - F_{i-1/2,j}) + \frac{1}{\Delta y} (G_{ij+1/2} - G_{ij-1/2}) = 0 \quad (3)$$

where q_{ij} is the cell averaged vector of dependant variables; $F_{i\pm 1/2,j}$ are the fluxes at the left and right cell boundaries, and $G_{ij\pm 1/2}$ are the fluxes at the bottom and top cell boundaries. Eq. (3) can be rewritten in the following form

$$\frac{dq}{dt} = \mathcal{E}(q) \quad (4)$$

where $\mathcal{E}(q)$ is the discrete operator representing the convective flux terms:

$$\mathcal{E}(q) = -\frac{1}{\Delta x} (F_{i+1/2,j} - F_{i-1/2,j}) - \frac{1}{\Delta y} (G_{ij+1/2} - G_{ij-1/2}). \quad (5)$$

Assuming that the numerical approximation for time level n is known, the optimal third-order total variation diminishing Runge–Kutta (TVDRK3) scheme is used to compute the numerical approximation for time level $n+1$, after the time step Δt , which is given as [56,57]:

$$\begin{aligned} q^{(1)} &= q^n + \Delta t \mathcal{E}(q^n) \\ q^{(2)} &= \frac{3}{4} q^n + \frac{1}{4} q^{(1)} + \frac{1}{4} \Delta t \mathcal{E}(q^{(1)}) \\ q^{n+1} &= \frac{1}{3} q^n + \frac{2}{3} q^{(2)} + \frac{2}{3} \Delta t \mathcal{E}(q^{(2)}) \end{aligned} \quad (6)$$

where Δt should be computed by

$$\Delta t = \min \left(\eta \frac{\Delta x}{\max(|\Lambda|)}, \eta \frac{\Delta y}{\max(|\Psi|)} \right) \quad (7)$$

in which $\max(|\Lambda|)$ and $\max(|\Psi|)$ represents the maximum absolute eigenvalues over the entire spatial domain at known time level. Here, $\eta \leq 1$ for numerical stability. In this study, we use $\eta = 0.5$ for all the computations. The TVDRK3 scheme has been extensively used to compute hyperbolic conservation laws (e.g., see [36,42,43,58–62]).

In the present study, a modular framework is designed for computing flux terms given by Eq. (3) in developing high-order accurate algorithms for hyperbolic conservation laws. The third-, fifth- and seventh-order variants of the weighted essentially non-oscillatory (WENO) method are considered and compared for their effectiveness and their ability to accurately compute the two-dimensional turbulent flows driven by the Kelvin–Helmholtz instability.

3.1. WENO reconstruction schemes

In the framework of reconstruction shock capturing schemes, for each cell, reconstructed left and right states are determined

and used to calculate fluxes at cell edges. Weighted essentially non-oscillatory (WENO) reconstruction is widely used interpolation method to construct left and right states at the cell boundaries from the solution available at the cell centers [43]. It consists of two basic procedures: (i) the selection of the interpolation procedure to estimate the solution at the interface boundaries from the solution available at the cell centers and (ii) the selection of the Riemann solver to determine the flux from the reconstructed left and right states at the cell boundaries. In the semi-discrete form given by Eq. (3) the fluxes at the interfaces are functions of left (bottom in y -direction) and right (top in y -direction) reconstructed states. In the following, we will omit the spatial index which is not in the direction of the action. We only present the schemes showing the procedures in x -direction, however, the same procedures are applied in y -direction.

3.1.1. WENO-3 reconstruction

The third-order WENO reconstruction can be written in the following form [40,41]

$$q_{i+1/2}^L = w_0 \left(-\frac{1}{2} q_{i-1} + \frac{3}{2} q_i \right) + w_1 \left(\frac{1}{2} q_i + \frac{1}{2} q_{i+1} \right) \quad (8)$$

$$q_{i-1/2}^R = w_0 \left(\frac{1}{2} q_i + \frac{1}{2} q_{i-1} \right) + w_1 \left(-\frac{1}{2} q_{i+1} + \frac{3}{2} q_i \right) \quad (9)$$

where nonlinear weights are defined as

$$w_k = \frac{\alpha_k}{\alpha_0 + \alpha_1}, \quad \alpha_k = \frac{d_k}{(\beta_k + \epsilon)^2}, \quad k = 0, 1 \quad (10)$$

in which the smoothness indicators are defined as

$$\beta_0 = (q_i - q_{i-1})^2 \quad (11)$$

$$\beta_1 = (q_{i+1} - q_i)^2 \quad (12)$$

where the larger this smoothness indicator β_k , the less smooth the function q is in the candidate stencil. Therefore, if there is a discontinuity in the stencil, its weight approaches to zero, and the other stencil becomes active for reconstructing the flux. Details about the design of the smoothness indicators have been given in Jiang and Shu [41]. Following [41], the optimal linear weighting coefficients are $d_0 = 1/3$ and $d_1 = 2/3$ in Eq. (8), and $d_0 = 2/3$ and $d_1 = 1/3$ in Eq. (9). It is typical to set $\epsilon = 10^{-6}$ for eliminating zero denominators. In this study, WENO-3 stands for the third-order WENO reconstruction scheme given by Eqs. (8) and (9).

3.1.2. WENO-5 reconstruction

The fifth-order WENO reconstruction for the left and right states is given as [41,43]

$$\begin{aligned} q_{i+1/2}^L &= w_0 \left(\frac{1}{3} q_{i-2} - \frac{7}{6} q_{i-1} + \frac{11}{6} q_i \right) \\ &\quad + w_1 \left(-\frac{1}{6} q_{i-1} + \frac{5}{6} q_i + \frac{1}{3} q_{i+1} \right) \\ &\quad + w_2 \left(\frac{1}{3} q_i + \frac{5}{6} q_{i+1} - \frac{1}{6} q_{i+2} \right) \end{aligned} \quad (13)$$

$$\begin{aligned} q_{i-1/2}^R &= w_0 \left(\frac{1}{3} q_i + \frac{5}{6} q_{i-1} - \frac{1}{6} q_{i-2} \right) \\ &\quad + w_1 \left(-\frac{1}{6} q_{i+1} + \frac{5}{6} q_i + \frac{1}{3} q_{i-1} \right) \\ &\quad + w_2 \left(\frac{1}{3} q_{i+2} - \frac{7}{6} q_{i+1} + \frac{11}{6} q_i \right) \end{aligned} \quad (14)$$

where nonlinear weights are defined as

$$w_k = \frac{\alpha_k}{\alpha_0 + \alpha_1 + \alpha_2}, \quad \alpha_k = \frac{d_k}{(\beta_k + \epsilon)^2}, \quad k = 0, 1, 2 \quad (15)$$

in which the smoothness indicators are defined as

$$\beta_0 = \frac{13}{12}(q_{i-2} - 2q_{i-1} + q_i)^2 + \frac{1}{4}(q_{i-2} - 4q_{i-1} + 3q_i)^2 \quad (16)$$

$$\beta_1 = \frac{13}{12}(q_{i-1} - 2q_i + q_{i+1})^2 + \frac{1}{4}(q_{i-1} - q_{i+1})^2 \quad (17)$$

$$\beta_2 = \frac{13}{12}(q_i - 2q_{i+1} + q_{i+2})^2 + \frac{1}{4}(3q_i - 4q_{i+1} + q_{i+2})^2 \quad (18)$$

Following [41], the optimal linear weighting coefficients are $d_0 = 1/10$, $d_1 = 3/5$, and $d_2 = 3/10$ in Eq. (13), and $d_0 = 3/10$, $d_1 = 3/5$, and $d_2 = 1/10$ in Eq. (14). Similarly, we also set $\epsilon = 10^{-6}$ to avoid division by zero. In this study, WENO-5 stands for the fifth-order WENO reconstruction scheme given by Eqs. (13) and (14). A rigorous mathematical analysis on the essential components of WENO schemes has been reported in [63], including analysis of the smoothness indicator along with the role of the ϵ parameter.

3.1.3. WENO-7 reconstruction

Reconstructed left and right states are determined by using the seventh-order WENO scheme in the following form [64]

$$\begin{aligned} q_{i+1/2}^L = & w_0 \left(-\frac{1}{4}q_{i-3} + \frac{13}{12}q_{i-2} - \frac{23}{12}q_{i-1} + \frac{25}{12}q_i \right) \\ & + w_1 \left(\frac{1}{12}q_{i-2} - \frac{5}{12}q_{i-1} + \frac{13}{12}q_i + \frac{1}{4}q_{i+1} \right) \\ & + w_2 \left(-\frac{1}{12}q_{i-1} + \frac{7}{12}q_i + \frac{7}{12}q_{i+1} - \frac{1}{12}q_{i+2} \right) \\ & + w_3 \left(\frac{1}{4}q_i + \frac{13}{12}q_{i+1} - \frac{5}{12}q_{i+2} + \frac{1}{12}q_{i+3} \right) \end{aligned} \quad (19)$$

$$\begin{aligned} q_{i-1/2}^R = & w_0 \left(\frac{1}{4}q_i + \frac{13}{12}q_{i-1} - \frac{5}{12}q_{i-2} + \frac{1}{12}q_{i-3} \right) \\ & + w_1 \left(-\frac{1}{12}q_{i+1} + \frac{7}{12}q_i + \frac{7}{12}q_{i-1} - \frac{1}{12}q_{i-2} \right) \\ & + w_2 \left(\frac{1}{12}q_{i+2} - \frac{5}{12}q_{i+1} + \frac{13}{12}q_i + \frac{1}{4}q_{i-1} \right) \\ & + w_3 \left(-\frac{1}{4}q_{i+3} + \frac{13}{12}q_{i+2} - \frac{23}{12}q_{i+1} + \frac{25}{12}q_i \right) \end{aligned} \quad (20)$$

where nonlinear weights are defined as

$$w_k = \frac{\alpha_k}{\alpha_0 + \alpha_1 + \alpha_2 + \alpha_3}, \quad \alpha_k = \frac{d_k}{(\beta_k + \epsilon)^2}, \quad k = 0, 1, 2, 3 \quad (21)$$

in which the smoothness indicators for the four-candidate-stencil case are defined as [64]

$$\begin{aligned} \beta_0 = & q_{i-3}(547q_{i-3} - 3882q_{i-2} + 4642q_{i-1} - 1854q_i) \\ & + q_{i-2}(7043q_{i-2} - 17246q_{i-1} + 7042q_i) \\ & + q_{i-1}(11003q_{i-1} - 9402q_i) + q_i(2107q_i) \end{aligned} \quad (22)$$

$$\begin{aligned} \beta_1 = & q_{i-2}(267q_{i-2} - 1642q_{i-1} + 1602q_i - 494q_{i+1}) \\ & + q_{i-1}(2843q_{i-1} - 5966q_i + 1922q_{i+1}) + q_i(3443q_i) \\ & - 2522q_{i+1}) + q_{i+1}(547q_{i+1}) \end{aligned} \quad (23)$$

$$\begin{aligned} \beta_2 = & q_{i-1}(547q_{i-1} - 2522q_i + 1922q_{i+1} - 494q_{i+2}) \\ & + q_i(3443q_i - 5966q_{i+1} + 1602q_{i+2}) \\ & + q_{i+1}(2843q_{i+1} - 1642q_{i+2}) + q_{i+2}(267q_{i+2}) \end{aligned} \quad (24)$$

$$\begin{aligned} \beta_3 = & q_i(2107q_i - 9402q_{i+1} + 7042q_{i+2} - 1854q_{i+3}) \\ & + q_{i+1}(11003q_{i+1} - 17246q_{i+2} + 4642q_{i+3}) \\ & + q_{i+2}(7043q_{i+2} - 3882q_{i+3}) + q_{i+3}(547q_{i+3}) \end{aligned} \quad (25)$$

Following [64], the optimal linear weights are given by $d_0 = 1/35$, $d_1 = 12/35$, $d_2 = 18/35$, and $d_3 = 4/35$ in Eq. (19), and $d_0 = 4/35$, $d_1 = 18/35$, $d_2 = 12/35$, and $d_3 = 1/35$ in Eq. (20).

Following [41], ϵ is taken as 10^{-6} in all cases. In this study, WENO-7 stands for the seventh-order WENO reconstruction scheme given by Eqs. (19) and (20).

3.2. Riemann solvers

After reconstructed left and right states are determined at cell edges by using WENO reconstruction procedures, Riemann solvers are adopted to calculate fluxes at these cell boundaries. In this study, we focus on the use of six different Riemann solvers and evaluate their performances through numerical experiments in various resolutions.

3.2.1. Rusanov scheme

Once left and right states are reconstructed the fluxes can be determined based on the maximum local wave propagation speed, Rusanov solver follows [65]

$$F_{i+1/2} = \frac{1}{2} \left(F^R + F^L \right) - \frac{c_{i+1/2}}{2} \left(q_{i+1/2}^R - q_{i+1/2}^L \right) \quad (26)$$

where F^R is the flux component using the right reconstructed state, $F^R = F(q_{i+1/2}^R)$, and F^L is the flux component using the left reconstructed state, $F^L = F(q_{i+1/2}^L)$, and $c_{i+1/2}$ is the local wave propagation speed which is the maximum absolute value of the eigenvalues corresponding to the Jacobian matrix of F between cells i and $i+1$ given by

$$c_{i+1/2} = \max(r(A_i), r(A_{i+1})) \quad (27)$$

where $r(A)$ represents the spectral radius of convective Jacobian matrix A . For the case of Euler equations, it can be simply written as $r(A) = \max(|u|, |u - a|, |u + a|)$. Thus, the wave propagation speed can be rewritten in the following form

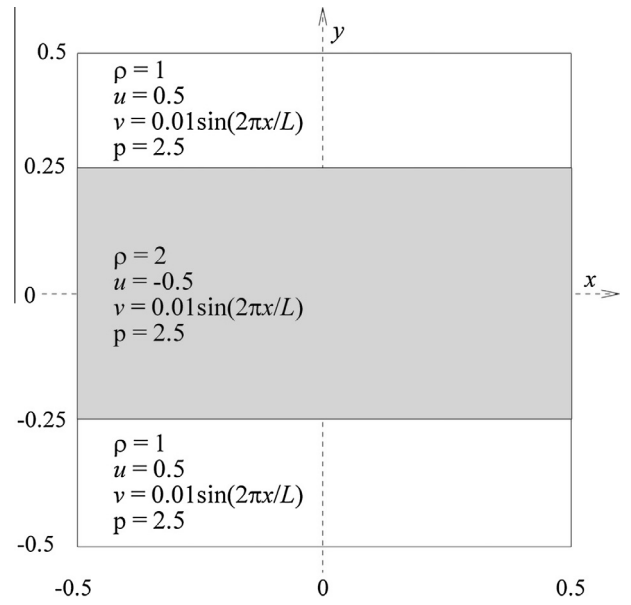


Fig. 1. Initial configuration of the Kelvin-Helmholtz instability test problem in a square periodic box whose edge has a length of $L = 1$. The ratio of specific heats is set to $\gamma = 1.4$ for all computations.

$$c_{i+1/2} = \max(|u|_i, |u - a|_i, |u + a|_i, |u|_{i+1}, |u - a|_{i+1}, |u + a|_{i+1}) \quad (28)$$

The above flux calculation is sometimes referred to as local Lax-Friedrichs flux [1,13,66]. There are other possibilities for estimating the wave propagation speed [36].

3.2.2. Roe scheme

According to the Godunov theorem [2], for a hyperbolic system of equations, if the Jacobian matrix of the flux vector is constant

(i.e., if A is constant), the exact values of fluxes at the interfaces can be computed by

$$F_{i+1/2} = \frac{1}{2} (F^R + F^L) - \frac{1}{2} R |A| L (q_{i+1/2}^R - q_{i+1/2}^L) \quad (29)$$

where $|A|$ is the diagonal matrix consisted of the absolute values of eigenvalues. In the system of Euler equations, however, the Jacobian matrix A is not constant (i.e., $A = A(q)$). The Roe solver [3], is an approximate Riemann solver based around the Godunov scheme

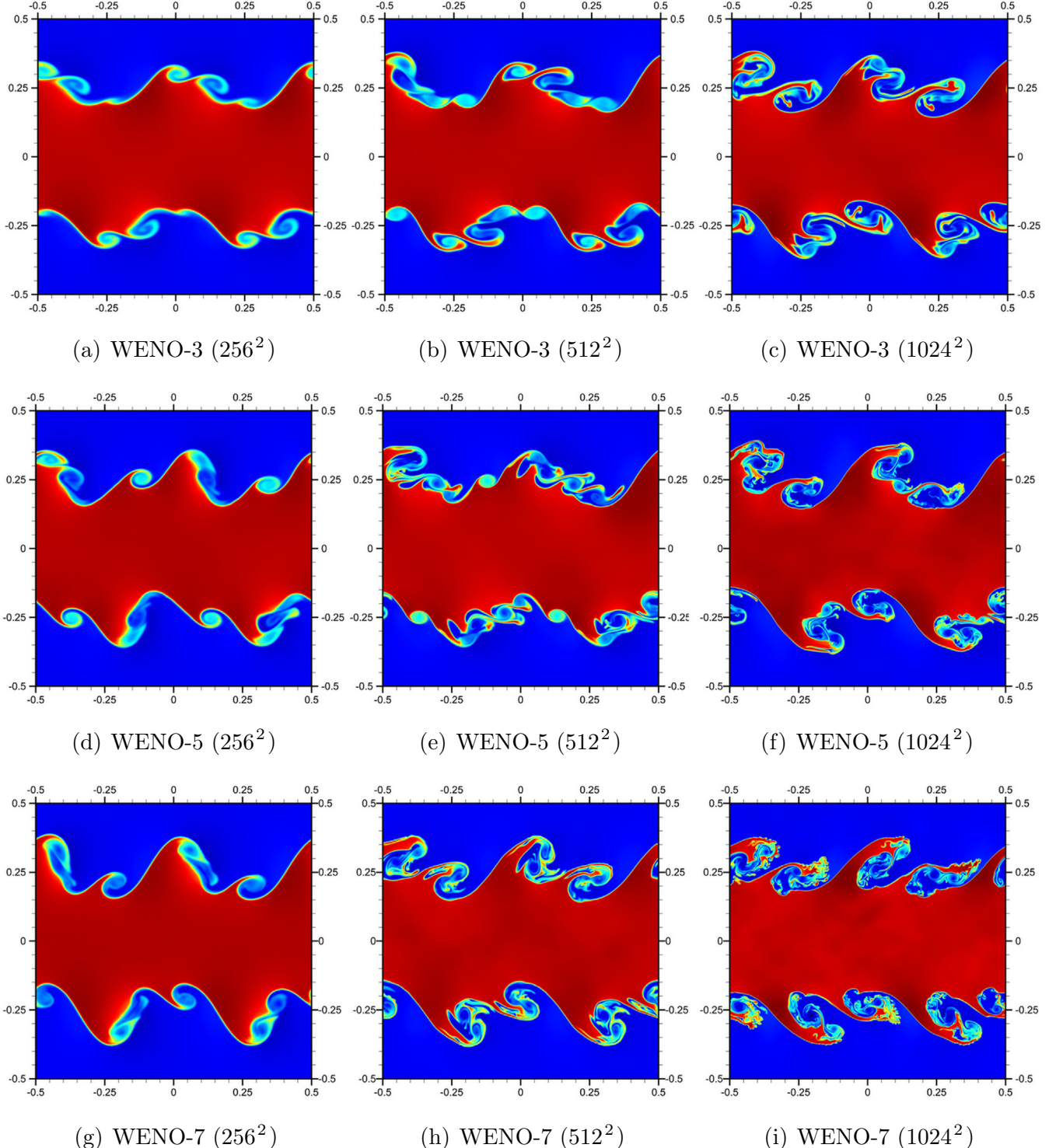


Fig. 2. Density contour plots at time $t = 1$ for the grid dependence study performed by using Roe's approximate Riemann solver.

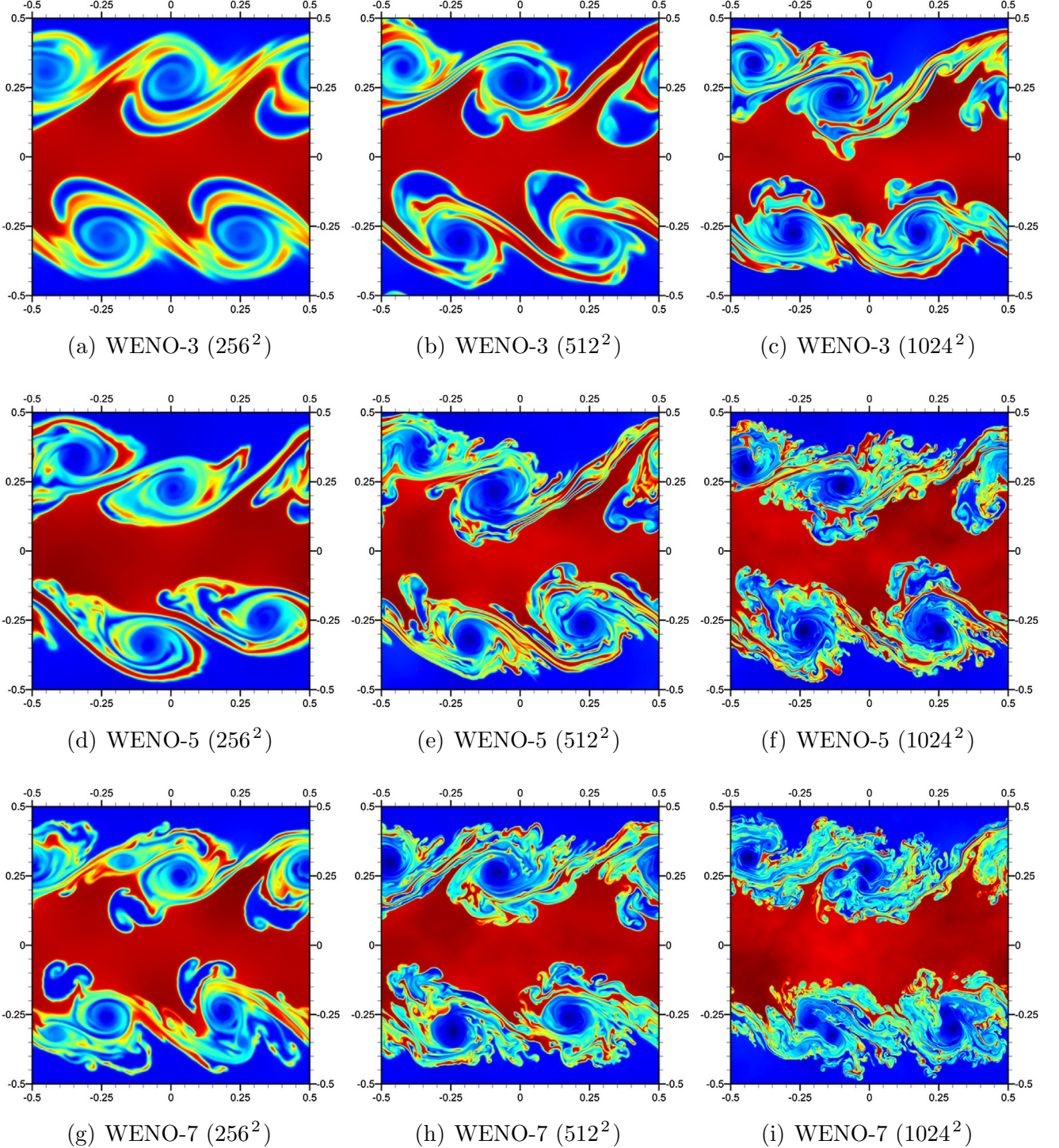


Fig. 3. Density contour plots at time $t = 3$ for the grid dependence study performed by using Roe's approximate Riemann solver.

and involves finding an estimate for the interface numerical flux as follows

$$F_{i+1/2} = \frac{1}{2} (F^R + F^L) - \frac{1}{2} \tilde{R} |\tilde{\lambda}| \tilde{L} (q_{i+1/2}^R - q_{i+1/2}^L) \quad (30)$$

where the tilde represents the Roe average (i.e., a density weighted average) between the left and right states. Specifically, the eigen-system matrices can be computed from the density averaged values given by

$$\tilde{u} = \frac{u_R \sqrt{\rho_R} + u_L \sqrt{\rho_L}}{\sqrt{\rho_R} + \sqrt{\rho_L}}, \quad (31)$$

$$\tilde{v} = \frac{v_R \sqrt{\rho_R} + v_L \sqrt{\rho_L}}{\sqrt{\rho_R} + \sqrt{\rho_L}}, \quad (32)$$

$$\tilde{H} = \frac{H_R \sqrt{\rho_R} + H_L \sqrt{\rho_L}}{\sqrt{\rho_R} + \sqrt{\rho_L}} \quad (33)$$

where the left and right states are available to us from the reconstruction formulas given in previous sections. The Roe averaged

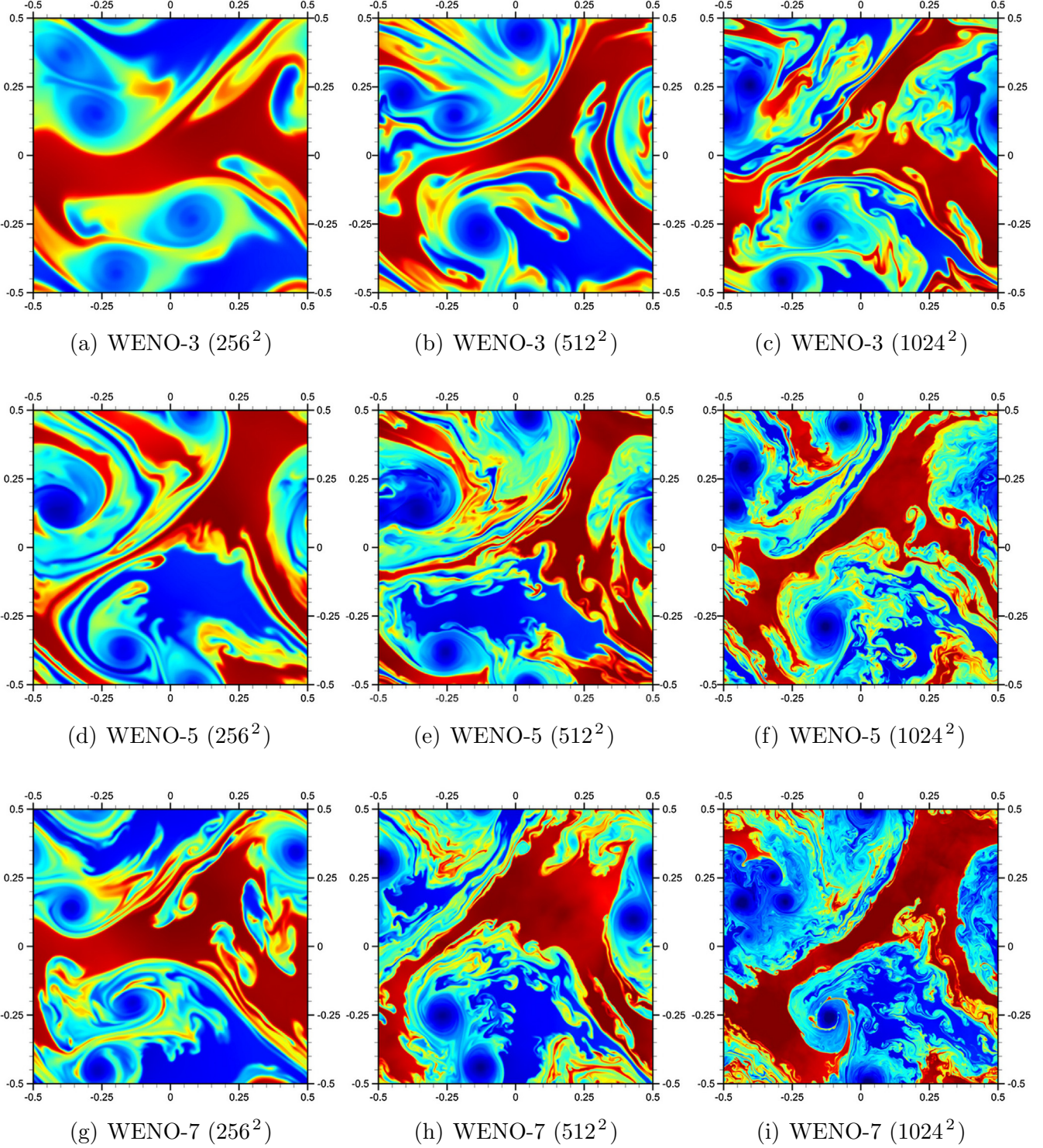


Fig. 4. Density contour plots at time $t = 5$ for the grid dependence study performed by using Roe's approximate Riemann solver.

speed of sound can be computed by using the state equations given by Eq. (2):

$$\tilde{a} = \sqrt{(\gamma - 1) \left[\tilde{H} - \frac{1}{2} (\tilde{u}^2 + \tilde{v}^2) \right]}. \quad (34)$$

It is realized that the stationary expansion shocks are not dissipated appropriately by this method. Harten [4] proposed the following

remedy to fix the entropy in the expansion shocks by replacing the Roe averaged eigenvalues with

$$|\tilde{\lambda}_i| = \begin{cases} |\tilde{\lambda}_i|, & \text{if } |\tilde{\lambda}_i| \geq 2\epsilon\tilde{a} \\ \tilde{\lambda}_i^2/(4\epsilon\tilde{a}) + \epsilon\tilde{a}, & \text{if } |\tilde{\lambda}_i| < 2\epsilon\tilde{a} \end{cases} \quad (35)$$

where \tilde{a} is the speed of the sound at averaged state. Here, $\tilde{\lambda}_1 = \tilde{\lambda}_2 = \tilde{u}$, $\tilde{\lambda}_3 = \tilde{u} + \tilde{a}$, and $\tilde{\lambda}_4 = \tilde{u} - \tilde{a}$ are the components of the

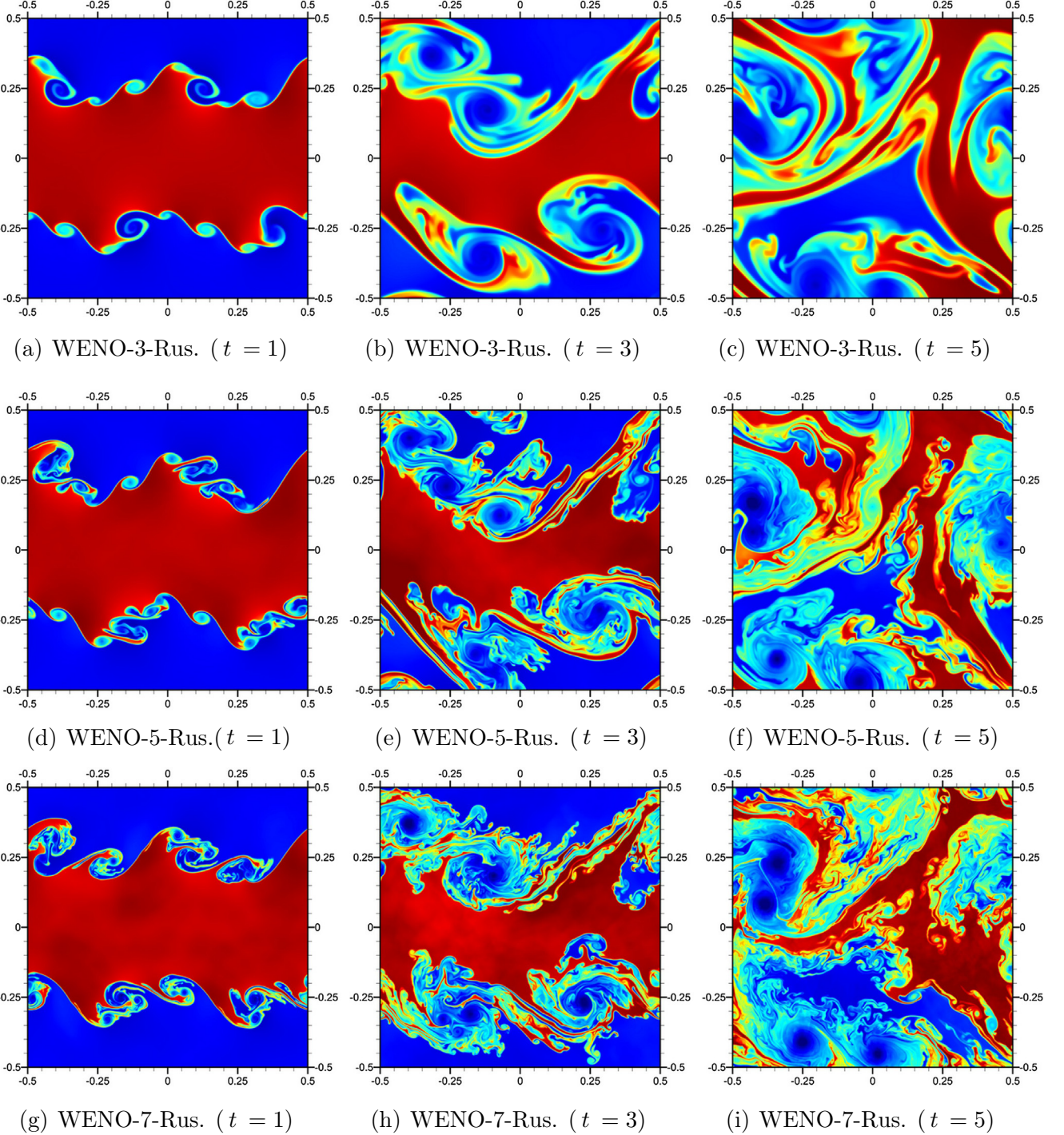


Fig. 5. Time evolution of the density field for the Kelvin–Helmholtz instability problem by using the Rusanov Riemann solver on a resolution of 1024^2 .

diagonal matrix A . Here, ε is a small positive number and is typically chosen as $\varepsilon = 0.1$ in our computations.

3.2.3. HLL scheme

Another vastly used approximate Riemann solver is due to Harten et al. [67]. They assumed that lower and upper bounds on the characteristics speeds can be used in the solution of Riemann problem involving the right and left states. In practice [13,68,69], these bounds are often approximated by

$$S_L = \min(u_L, u_R) - \max(a_L, a_R) \quad (36)$$

$$S_R = \max(u_L, u_R) + \max(a_L, a_R) \quad (37)$$

where S_L and S_R are lower and upper bounds on the left and right state characteristics speeds. The HLL approximate Riemann solver takes the form

$$F_{i+1/2} = \begin{cases} F^L, & \text{if } S_L \geq 0 \\ F^R, & \text{if } S_R \leq 0 \\ \frac{S_R F^L - S_L F^R + S_L S_R (q_{i+1/2}^R - q_{i+1/2}^L)}{S_R - S_L}, & \text{otherwise.} \end{cases} \quad (38)$$

3.2.4. FORCE scheme

The first order centered (FORCE) scheme is obtained by averaging the Lax–Friedrichs and Richtmyer flux schemes [13,70,71]. In

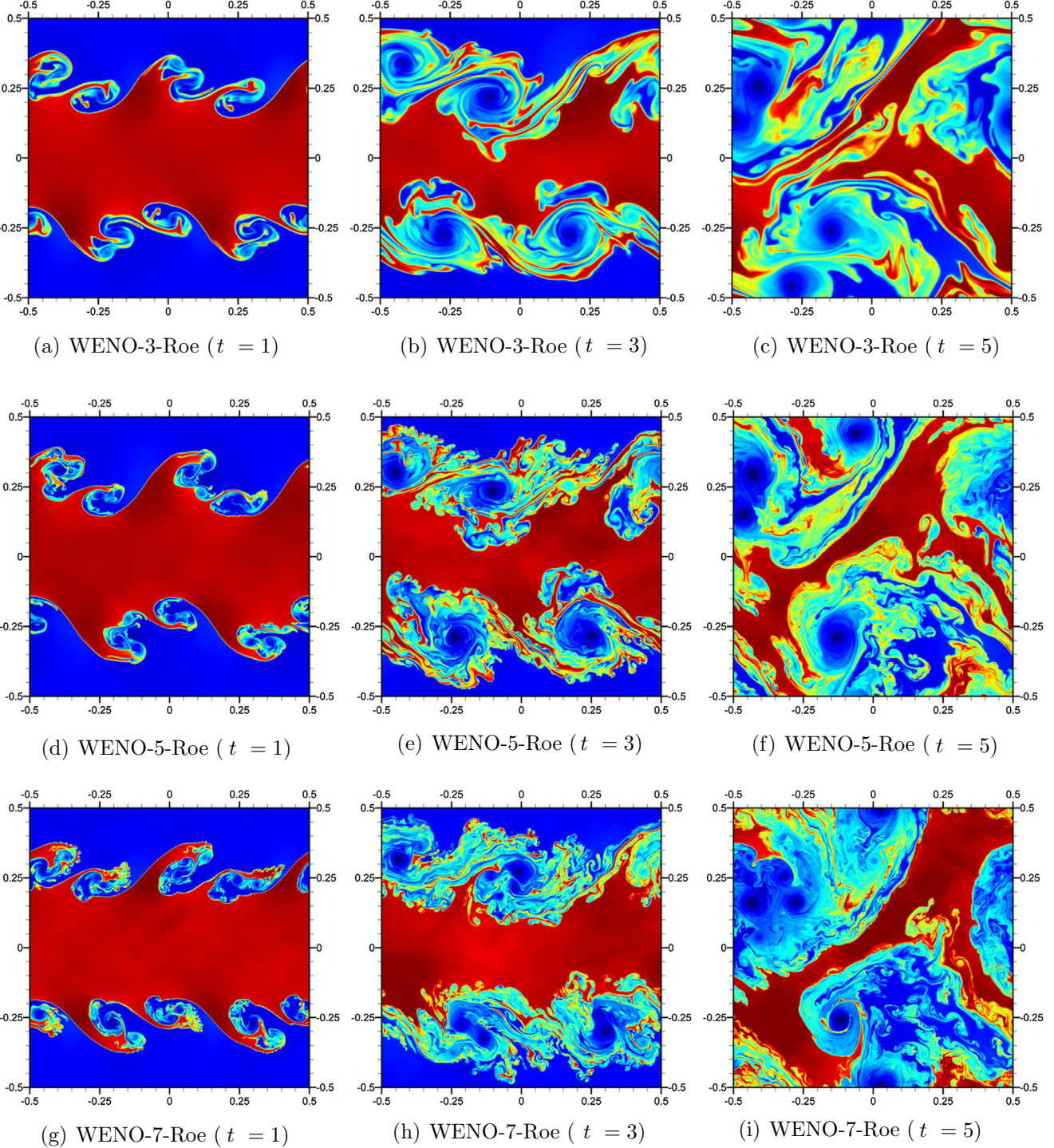


Fig. 6. Time evolution of the density field for the Kelvin–Helmholtz instability problem by using the Roe Riemann solver on a resolution of 1024^2 .

the Lax–Friedrichs scheme, the numerical flux at the interface becomes

$$F_{i+1/2}^{LF} = \frac{1}{2} \left((F^R + F^L) - \frac{\Delta x}{\Delta t} (q_{i+1/2}^R - q_{i+1/2}^L) \right) \quad (39)$$

and the Richtrmyer flux can be computed by using the intermediate conservative quantities given by

$$q_{i+1/2}^{RL} = \frac{1}{2} \left((q_{i+1/2}^R + q_{i+1/2}^L) - \frac{\Delta t}{\Delta x} (F^R - F^L) \right), \quad F_{i+1/2}^{RI} = F(q_{i+1/2}^{RL}) \quad (40)$$

and finally the FORCE flux is

$$F_{i+1/2} = \frac{1}{2} \left(F_{i+1/2}^{LF} + F_{i+1/2}^{RI} \right). \quad (41)$$

3.2.5. AUSM scheme

The AUSM was proposed by Liou and Steffen [72] and stands for Advection Upstream Splitting Method. It was motivated to provide an alternative approach to low-diffusion flux-splitting methods by recognizing that the inviscid flux consist of two physically distinct parts (i.e., convective and pressure fluxes). A cell-interface advection Mach number is appropriately defined to determine convective flow quantities. Many variants of the AUSM have been proposed to yield a more accurate and robust version in all-speed

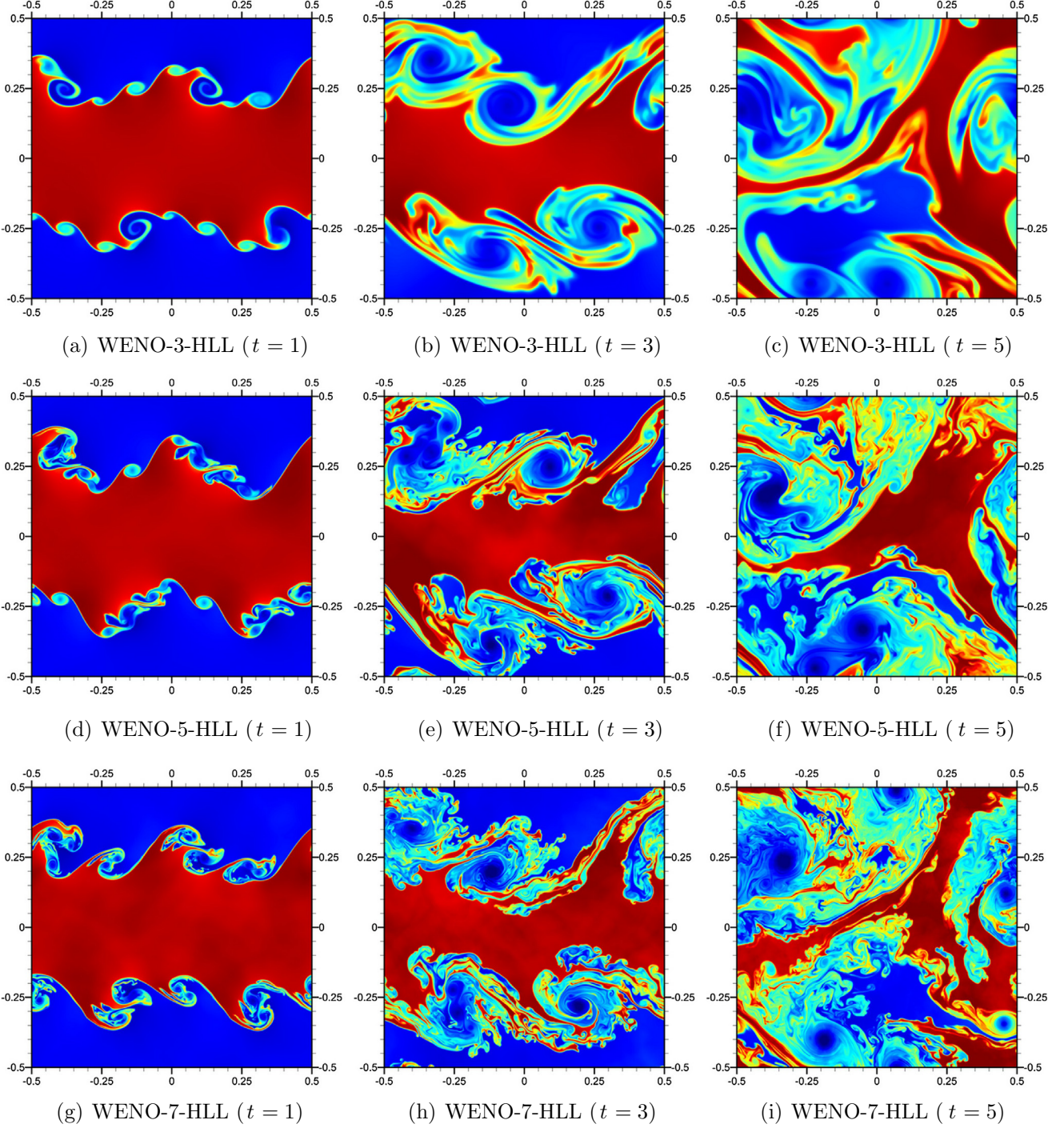


Fig. 7. Time evolution of the density field for the Kelvin–Helmholtz instability problem by using the HLL Riemann solver on a resolution of 1024^2 .

regimes [73–78]. Here, we use the AUSM as a low-diffusion Riemann solver between the right and left reconstructed states yielding the interface numerical flux as

$$F_{i+1/2} = \frac{M_{i+1/2}}{2} \left[\begin{pmatrix} \rho a \\ \rho a u \\ \rho a v \\ \rho a H \end{pmatrix}_L + \begin{pmatrix} \rho a \\ \rho a u \\ \rho a v \\ \rho a H \end{pmatrix}_R \right] - \frac{|M_{i+1/2}|}{2} \left[\begin{pmatrix} \rho a \\ \rho a u \\ \rho a v \\ \rho a H \end{pmatrix}_R - \begin{pmatrix} \rho a \\ \rho a u \\ \rho a v \\ \rho a H \end{pmatrix}_L \right] + \begin{pmatrix} 0 \\ p_L^+ + p_R^- \\ 0 \\ 0 \end{pmatrix} \quad (42)$$

where

$$M_{i+1/2} = M_L^+ + M_R^- \quad (43)$$

in which the directional convective Mach number (i.e., $M = u/a$ in x -direction) is given as

$$M^\pm = \begin{cases} \pm \frac{1}{4}(M \pm 1)^2, & \text{if } |M| \leq 1 \\ \frac{1}{2}(M \pm |M|), & \text{otherwise} \end{cases} \quad (44)$$

and we use the following split formula for the pressure,

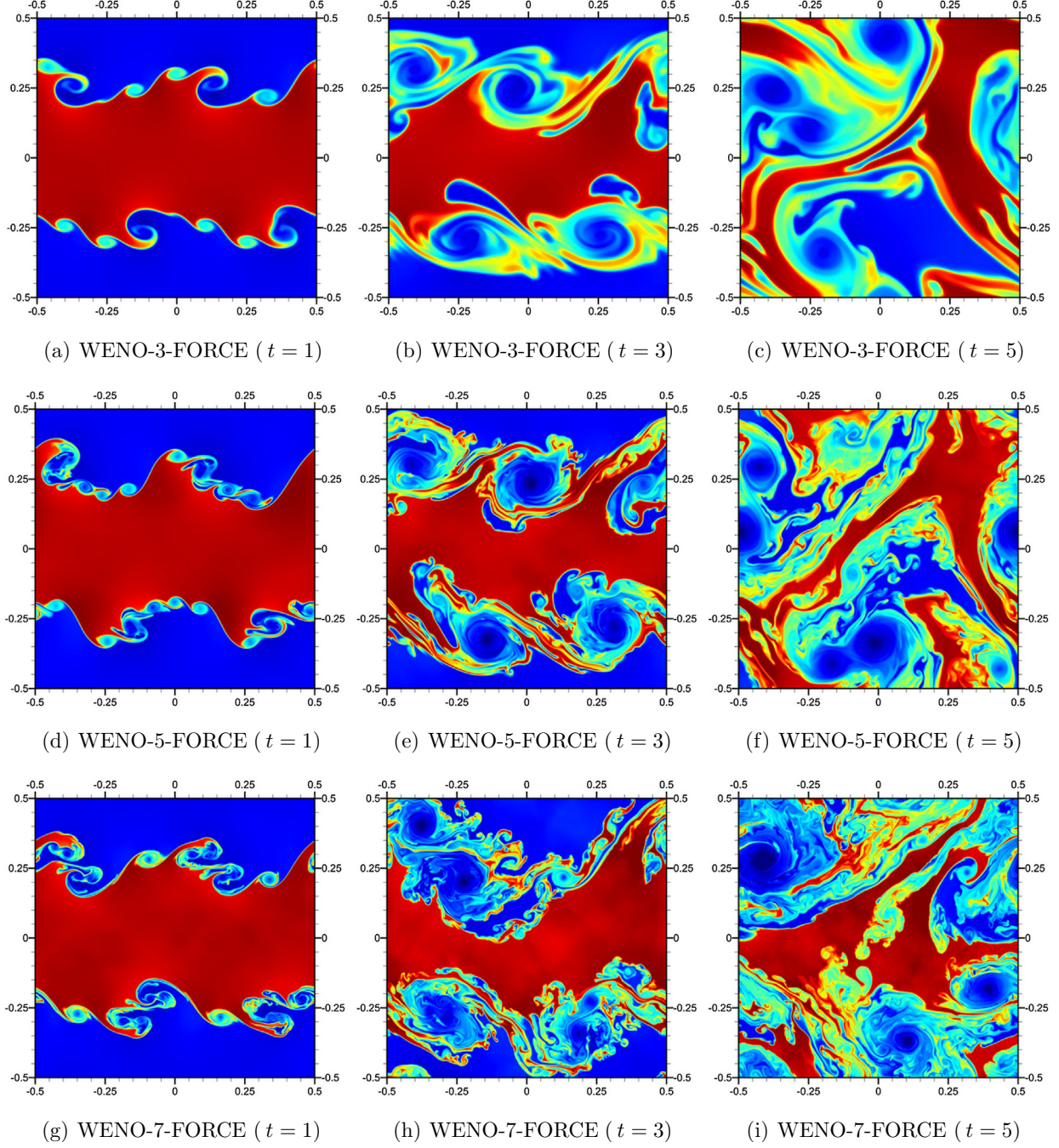


Fig. 8. Time evolution of the density field for the Kelvin–Helmholtz instability problem by using the FORCE Riemann solver on a resolution of 1024^2 .

$$p^\pm = \begin{cases} p \frac{1}{4}(M \pm 1)^2(2 \mp M), & \text{if } |M| \leq 1 \\ p \frac{1}{2}(M \pm |M|)/M, & \text{otherwise.} \end{cases} \quad (45)$$

3.2.6. Marquina scheme

To compute the numerical flux at a cell interface we include the following characteristic-based scheme in our comparisons [79,80];

$$F_{i+1/2} = [R]^L \{\phi^+\} + [R]^R \{\phi^-\} \quad (46)$$

where $[R]^{R,L}$ is the right eigenvector matrix computed from the right or left reconstructed state variables. To compute $\{\phi^\pm\}$ Marquina scheme follows:

```

For k = 1, ..., 4
  if sign(1, λ_k^L λ_k^R) = 1 then
    if λ_k^L > 0 then
      φ_k^+ = φ_k^L, and φ_k^- = 0
    else
      φ_k^+ = 0, and φ_k^- = φ_k^R
    end if
  else
    α_k = max(|λ_k^L|, |λ_k^R|)
    φ_k^+ = 1/2(φ_k^L + α_k ω_k^L)
    φ_k^- = 1/2(φ_k^R - α_k ω_k^R)
  end if

```

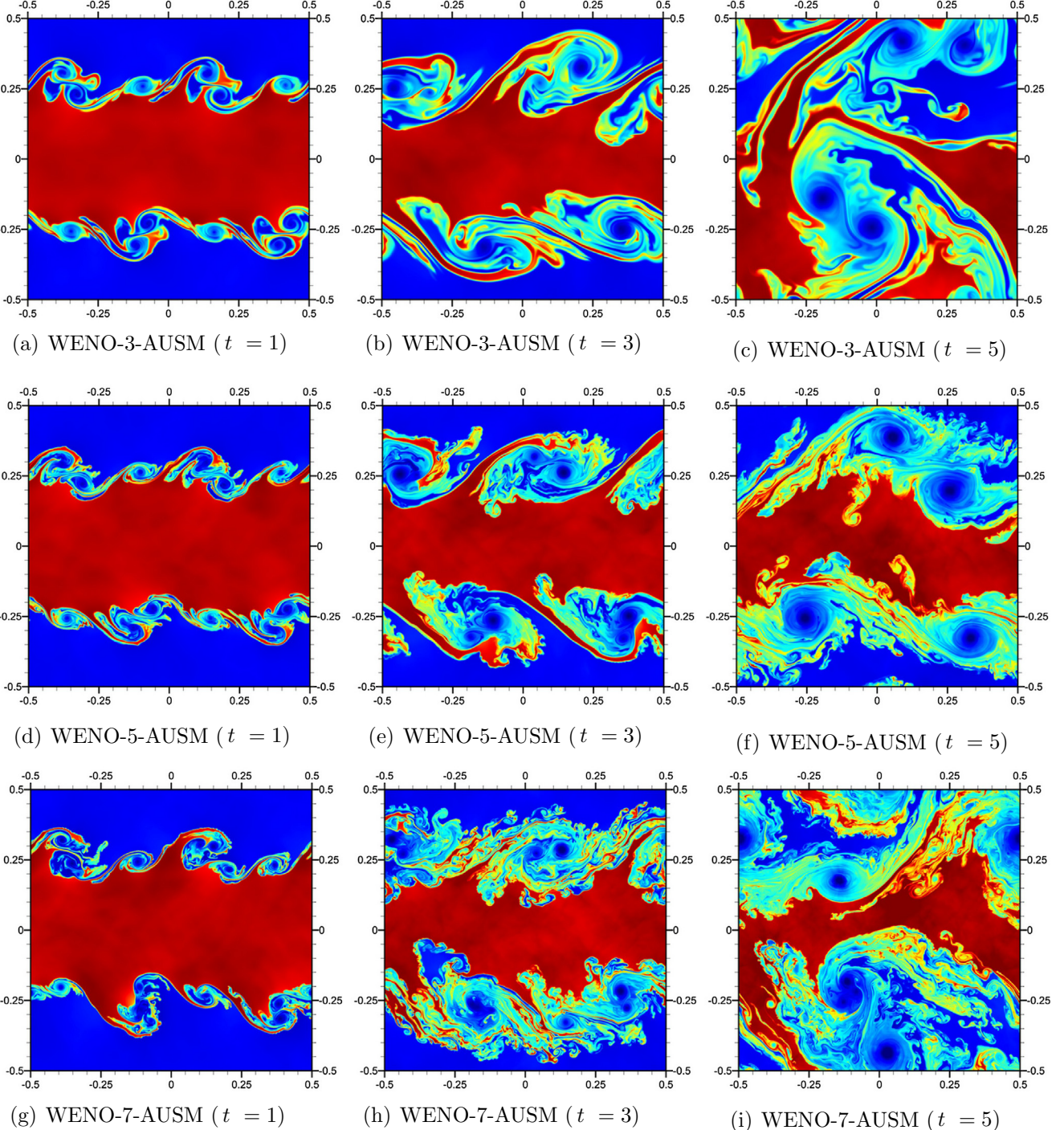


Fig. 9. Time evolution of the density field for the Kelvin–Helmholtz instability problem by using the AUSM Riemann solver on a resolution of 1024^2 .

where ϕ_k and ω_k at the left and right states can easily be computed by projecting the left eigenvector matrix $[L]$ onto flux and conservative variable vectors, i.e., $\{\phi\}^{R,L} = [L]^{R,L}\{F\}^{R,L}$ and $\{\omega\}^{R,L} = [L]^{R,L}\{q\}^{R,L}$. Here, $\text{sign}(a, b)$ returns the value of a with the sign of b . The eigenvector matrices (i.e., $[R]$ and $[L]$), are defined in [36].

4. Results

In this section, the performance of joint solvers is analyzed by systematic comparisons for various resolutions. Numerical assessments on dissipative characteristics of these solvers are presented

by simulations of the Kelvin–Helmholtz instability problem using a single mode perturbation initial condition in two-dimensions [81,82]. This test problem demonstrates the solvers' ability to evolve a linear perturbation into two-dimensional turbulence. As a result of the relatively low diffusion of the high-order numerical schemes, the Kelvin–Helmholtz instability triggers to generate small-scale vortical structures at the sharp density interfaces [36] and these vortices freely evolve with time and interact with each other forming a two-dimensional turbulence regime. Since this turbulence is restricted to two-dimensions, these vortices slowly become bigger vortices with time by a vortex merging mechanism (e.g., see [83,84]).

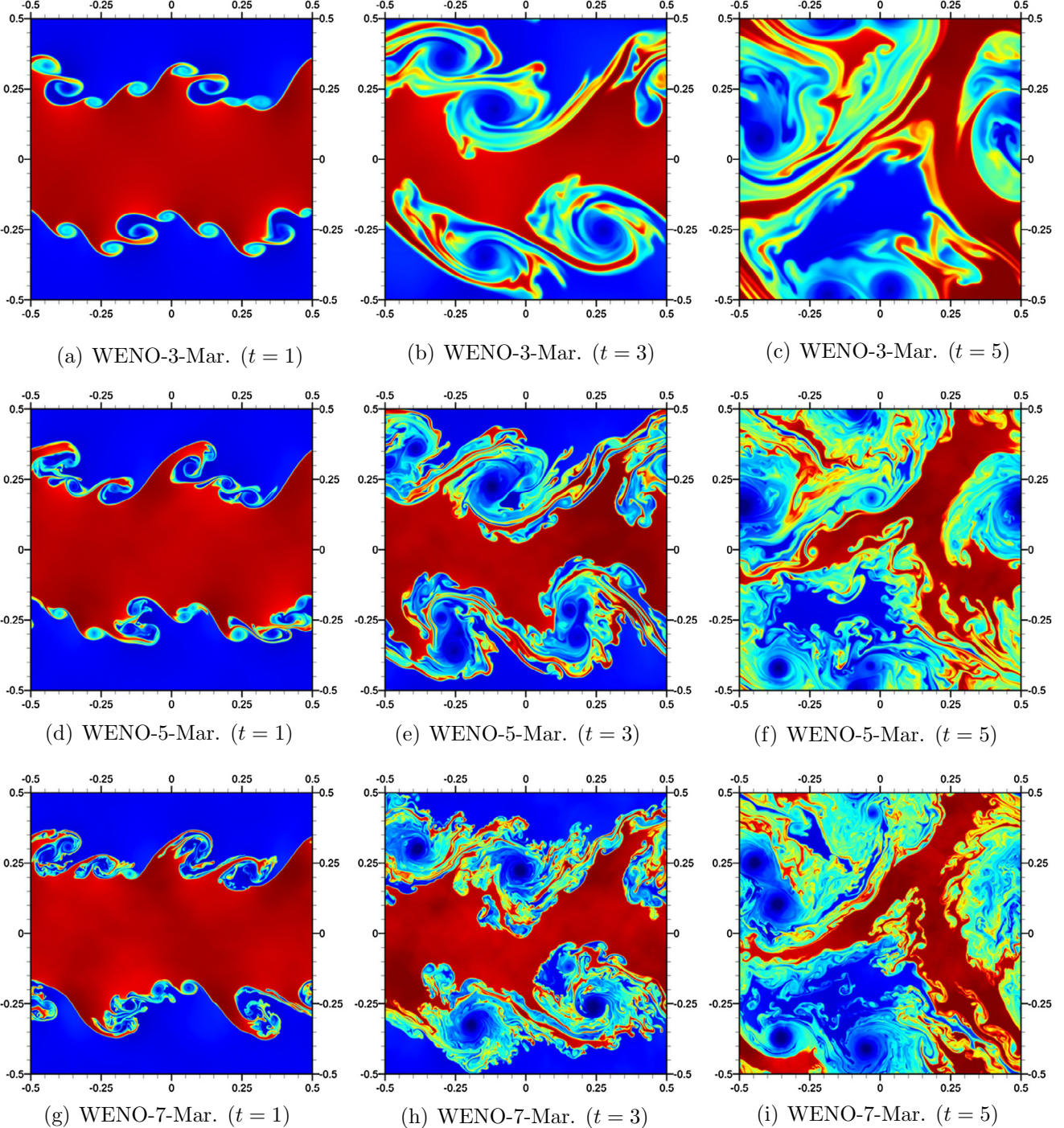


Fig. 10. Time evolution of the density field for the Kelvin–Helmholtz instability problem by using the Marquina Riemann solver on a resolution of 1024^2 .

Fig. 1 describes initial conditions for the Kelvin–Helmholtz instability problem. The computational domain is a square box with sides of length $L = 1$. Periodic boundary conditions are applied in both directions. Initial pressure is given as $p = 2.5$ everywhere. The ratio of specific heats is set to $\gamma = 1.4$ for all computations. Initially, density and the horizontal component of the velocity values are set to $\rho = 1$ and $u = 0.5$ in the outer region $|y| \geq 0.25$; $\rho = 2$ and $u = -0.5$ in the inner region $|y| < 0.25$, respectively. We perturb the vertical component of velocity by using a single mode perturbation, which the perturbation is a sine wave with one wavelength in the x dimension. The amplitude of

the perturbation is set to $\delta = 0.01$. All numerical experiments conducted here are solved for a maximum dimensionless time of $t = 5$. Similar configuration for the Kelvin–Helmholtz instability problem has been also presented in the Athena code hydrodynamics test suite developed by Stone et al. [85].

We evaluate the performance of the joint solvers by performing computations for three different equally-spaced Cartesian meshes with spatial resolutions of 256^2 , 512^2 , and 1024^2 . Comparing the third-, fifth- and seventh-order WENO schemes, Figs. 2–4 illustrate the density fields on these resolutions by using Roe's approximate Riemann solver at time instants $t = 1$, $t = 3$, and $t = 5$, respectively.

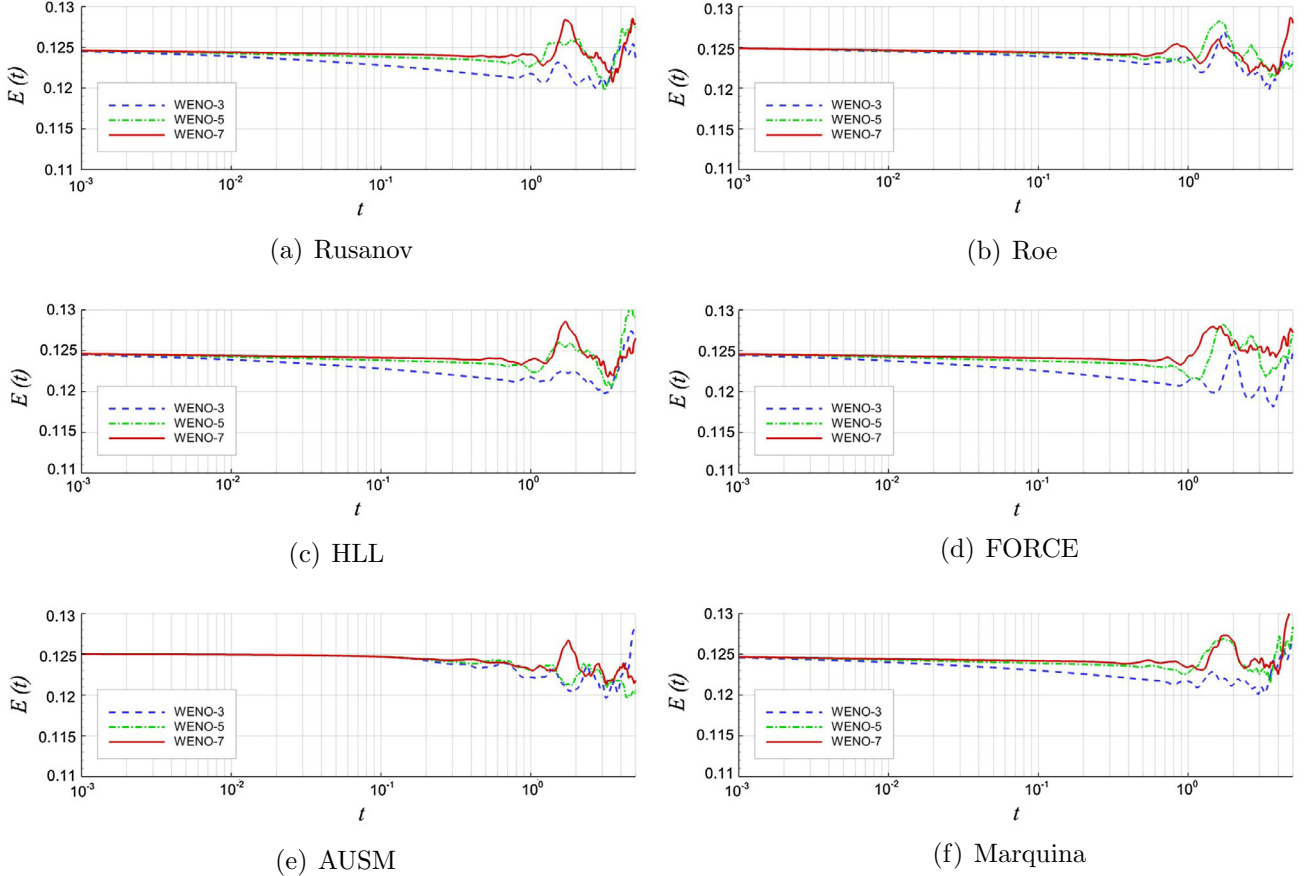


Fig. 11. Time histories of total energy $E(t)$ for solving the Kelvin–Helmholtz instability by using various Riemann flux formulas on a resolution of 1024^2 .

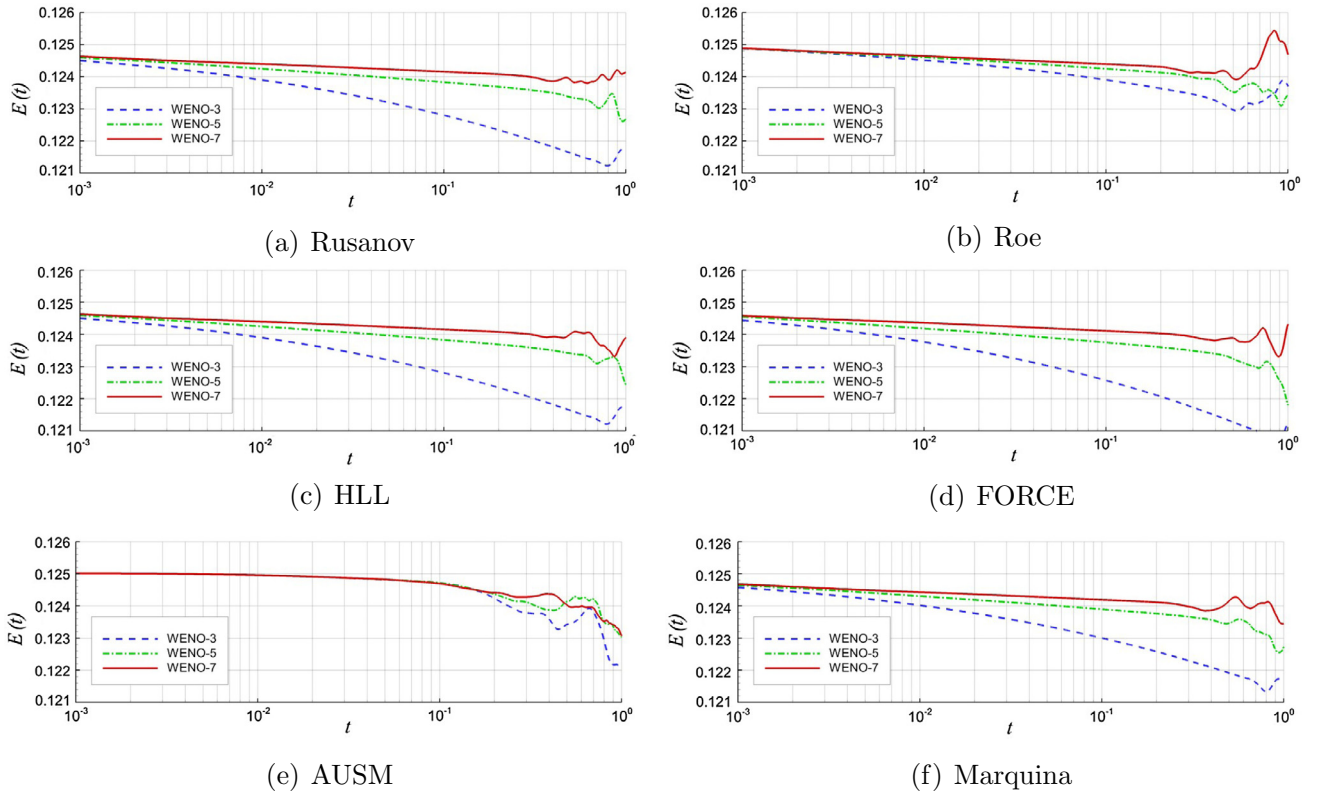


Fig. 12. Zoomed view of time histories of total energy $E(t)$ for solving the Kelvin–Helmholtz instability by using various Riemann flux formulas on a resolution of 1024^2 .

It can be seen that the higher-order formulations provide much better resolving property than that of the lower-order formulations. The small scale vortical structures are generated and captured by the fifth- and seventh-order WENO schemes yielding two-dimensional turbulence with time. As we can see, a filamentation process occurs, generated small scale vortices triggered by the Kelvin–Helmholtz initially at discontinuous interfaces start to interact with each other and become bigger vortices with time by a vortex merging mechanism. However, the degree of filamentation is bigger for both higher resolution and higher reconstruction of the WENO scheme.

Next, we present results obtained by sixth different Riemann solvers explained in Section 3.2. Fig. 5 shows the evolution of density field for various order reconstruction WENO schemes by using the Rusanov scheme. Similar comparisons are plotted in Fig. 6 for the Roe scheme; in Fig. 7 for the HLL scheme; in Fig. 8 for the FORCE scheme; in Fig. 9 for the AUSM scheme; and Fig. 10 for the Marquina scheme. Among them the FORCE Riemann solver seems to be most dissipative. The most accurate results are obtained with the Roe and AUSM Riemann solvers, followed by the HLL, Rusanov and Marquina solvers. We also note that there is no significant difference between FORCE, HLL, Rusanov and Marquina solvers due to high numerical damping. However, Roe and AUSM scheme provide less numerical dissipation yielding more filamentation processes. We demonstrate that the results highly depend on the selection of the Riemann solver as well as the degree of the numerical reconstruction in which higher-order schemes generates less numerical dissipation.

In addition to these density field plots, we also present the time histories of total energy $E(t) = \frac{1}{2}(u^2 + v^2)$ in order to quantify the dissipative characteristics of the joint solvers. Fig. 11 shows $E(t)$ in log–log graphs for the Riemann solvers tested in this study. The close-up representations in initial times are also illustrated in Fig. 12. Among the Riemann solvers considered, the AUSM scheme yields the most accurate results showing the least amount of numerical dissipation, although the Roe scheme also produces accurate results without excessive dissipation. FORCE scheme produces overly-dissipative results followed by HLL, Rusanov and Marquina schemes. It can be seen that order of the reconstruction

scheme has crucial effects on dissipative behavior. Although the most accurate results are obtained with the seventh-order WENO reconstruction, the fifth-order reconstruction also yields similar results which are considerably more accurate than those of obtained by the third-order reconstruction scheme.

In order to examine the characteristics of two-dimensional turbulence we compute the energy spectrum in wave space using fast Fourier transform (i.e., see [83] for more details). It is known from the KBL theory that the energy spectrum in the inertial range approaches the classical k^{-3} scaling. Figs. 13–15, show energy spectra computed by the WENO-3, WENO-5, and WENO-7

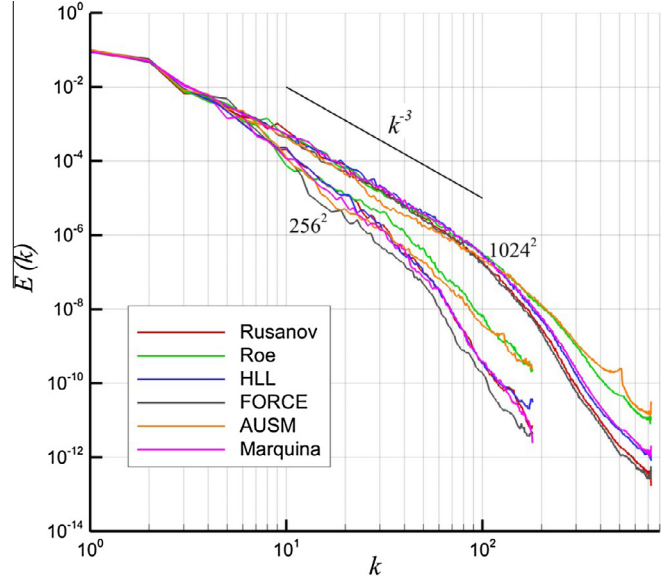


Fig. 14. Comparison of the angle averaged energy spectrum computed by the WENO-5 reconstruction scheme equipped with various Riemann flux formulas at time $t = 5$. The angle averaged energy spectrum in the inertial range flattens towards the classical k^{-3} scaling, in agreement with the KBL theory of two-dimensional turbulence.

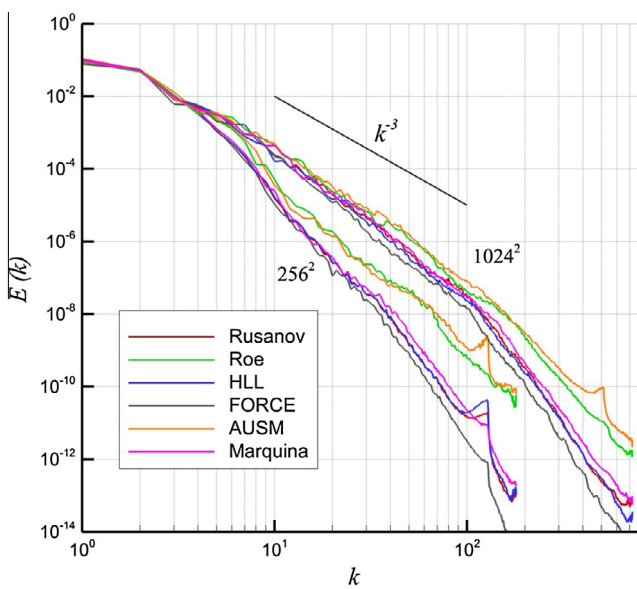


Fig. 13. Comparison of the angle averaged energy spectrum computed by the WENO-3 reconstruction scheme equipped with various Riemann flux formulas at time $t = 5$. The angle averaged energy spectrum in the inertial range flattens towards the classical k^{-3} scaling, in agreement with the KBL theory of two-dimensional turbulence.

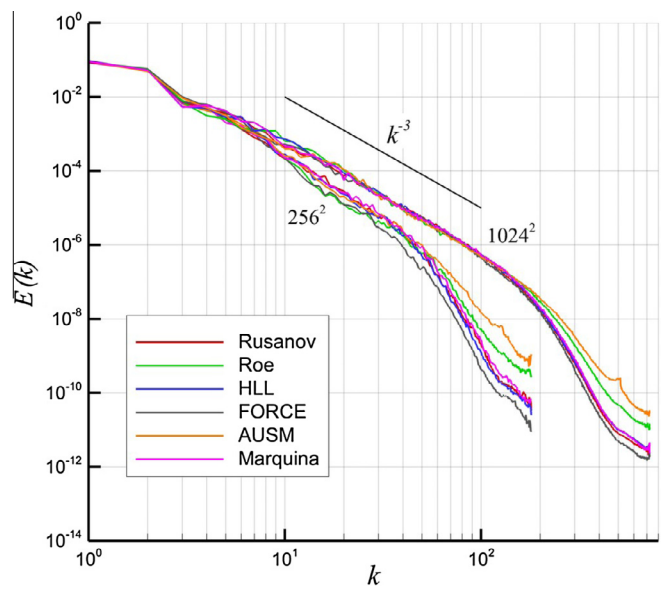


Fig. 15. Comparison of the angle averaged energy spectrum computed by the WENO-7 reconstruction scheme equipped with various Riemann flux formulas at time $t = 5$. The angle averaged energy spectrum in the inertial range flattens towards the classical k^{-3} scaling, in agreement with the KBL theory of two-dimensional turbulence.

Table 1

Energy densities and scaling exponent α of the energy spectrum $E(k)$ measured at time $t = 5$ for solving the Kelvin–Helmholtz instability problem on a resolution of 256^2 using the shock capturing schemes used in this study.

	WENO-3			WENO-5			WENO-7		
	$E(10)$	$E(100)$	α	$E(10)$	$E(100)$	α	$E(10)$	$E(100)$	α
Rusanov	1.52E–05	1.37E–11	6.05	2.06E–04	3.51E–10	5.77	2.10E–04	2.08E–09	5.01
Roe	5.11E–05	6.19E–10	4.92	7.53E–05	7.25E–09	4.02	2.09E–04	5.41E–09	4.59
HLL	1.64E–05	1.87E–11	5.94	2.33E–04	3.85E–10	5.78	2.76E–04	1.28E–09	5.33
FORCE	1.07E–05	3.16E–12	6.53	1.20E–04	1.86E–10	5.81	2.19E–04	4.17E–10	5.72
AUSM	3.48E–05	1.22E–09	4.45	1.28E–04	3.76E–09	4.53	2.52E–04	1.48E–08	4.23
Marquina	2.56E–05	2.13E–11	6.08	1.13E–04	4.08E–10	5.44	2.25E–04	2.76E–09	4.91

Table 2

Energy densities and scaling exponent α of the energy spectrum $E(k)$ measured at time $t = 5$ for solving the Kelvin–Helmholtz instability problem on a resolution of 512^2 using the shock capturing schemes used in this study.

	WENO-3			WENO-5			WENO-7		
	$E(10)$	$E(100)$	α	$E(10)$	$E(100)$	α	$E(10)$	$E(100)$	α
Rusanov	1.21E–04	1.69E–09	4.85	3.21E–04	1.42E–08	4.35	3.00E–04	1.06E–07	3.45
Roe	1.65E–04	2.65E–08	3.79	4.32E–04	5.90E–08	3.86	4.37E–04	1.06E–07	3.61
HLL	1.04E–04	8.24E–10	5.10	2.81E–04	1.72E–08	4.21	5.26E–04	7.84E–08	3.83
FORCE	9.79E–05	2.62E–10	5.57	2.79E–04	9.77E–09	4.46	5.05E–04	6.90E–08	3.86
AUSM	1.81E–04	8.95E–09	4.31	4.15E–04	5.65E–08	3.87	4.55E–04	1.26E–07	3.56
Marquina	1.14E–04	2.40E–09	4.68	2.79E–04	2.80E–08	4.00	4.29E–04	9.51E–08	3.65

Table 3

Energy densities and scaling exponent α of the energy spectrum $E(k)$ measured at time $t = 5$ for solving the Kelvin–Helmholtz instability problem on a resolution of 1024^2 using the shock capturing schemes used in this study.

	WENO-3			WENO-5			WENO-7		
	$E(10)$	$E(100)$	α	$E(10)$	$E(100)$	α	$E(10)$	$E(100)$	α
Rusanov	2.39E–04	3.27E–08	3.86	6.73E–04	1.97E–07	3.53	4.45E–04	5.17E–07	2.94
Roe	4.51E–04	4.17E–08	4.03	4.27E–04	2.97E–07	3.16	6.34E–04	4.93E–07	3.11
HLL	1.61E–04	2.35E–08	3.84	4.40E–04	3.26E–07	3.13	7.25E–04	5.36E–07	3.13
FORCE	2.22E–04	1.51E–08	4.17	5.20E–04	1.96E–07	3.42	5.31E–04	4.53E–07	3.07
AUSM	5.02E–04	7.77E–08	3.81	4.48E–04	2.46E–07	3.26	3.97E–04	4.53E–07	2.94
Marquina	4.38E–04	2.71E–08	4.21	5.35E–04	2.96E–07	3.26	4.65E–04	5.10E–07	2.96

Table 4

The total CPU costs (in hours) for solving the Kelvin–Helmholtz instability problem at time $t = 1$ by using various order WENO reconstruction schemes equipped with six different Riemann solvers considered in this study.

Reconstruction	Rusanov	Roe	HLL	FORCE	AUSM	Marquina
256^2						
WENO-3	0.1695	0.2475	0.1764	0.1692	0.1854	0.2270
WENO-5	0.2396	0.3167	0.2473	0.2348	0.2557	0.2969
WENO-7	0.3590	0.4353	0.3665	0.3517	0.3863	0.4188
512^2						
WENO-3	1.5432	2.2436	1.7285	1.6969	1.6136	1.9997
WENO-5	2.1513	2.7588	2.1879	2.1369	2.2257	2.6726
WENO-7	3.1790	3.7677	3.1901	3.1009	3.3181	3.6927
1024^2						
WENO-3	12.7595	17.5507	12.8741	12.8236	13.6887	16.6842
WENO-5	18.4537	22.8516	18.4003	17.7486	19.0516	22.7735
WENO-7	27.5628	34.7425	27.3946	26.6776	27.4658	31.2851

reconstruction schemes, respectively. In these figures, the angle averaged energy spectra are illustrated for the approximate Riemann solvers tested in this study. More quantitative results are tabulated in Tables 1–3, measuring the energy densities at $k = 10$ and $k = 100$ as well as scaling exponents. First, we observe that energy spectra are steeper for low resolution computations and approaches k^{-3} scaling as the resolution increases. Second, these figures demonstrate that the energy spectra converge to k^{-3} scaling in the inertial range for increasing the order of the reconstruction scheme. Intercomparisons of the Riemann solvers

clearly demonstrate that the FORCE scheme yields overly-dissipated results, whereas the AUSM scheme results in the least numerical dissipation. Roe scheme also performs very well without having an excessive dissipation. There is no significant difference among HLL, Rusanov and Marquina schemes. In the inertial range, especially for the fifth- and seventh-order WENO reconstruction schemes, it is also interesting to see that energy spectra scale as k^{-3} and are invariant of the approximate Riemann solver used. Having a third-order reconstruction scheme, Fig. 13 also illustrates that a higher degree of pile-up phenomenon occurs in the energy

spectra for all the approximate Riemann solvers except the Roe and overly-dissipative FORCE schemes.

Finally, we present the computational efficiencies of the schemes considered in this study. All computations were carried out using the gfortran compiler on a Linux cluster system made up of quad-core Intel Xeon X5355 (2.66 GHz/node). The total CPU costs (in hours) for the third-, fifth- and seventh-order WENO reconstruction schemes which are listed in Table 4 for various resolutions. Among the Riemann solvers, due to its simplicity Rusanov solver is the most efficient one, followed by FORCE, HLL, AUSM, Marquina and Roe solvers. Although we have not attempted any special efforts for writing optimal code, we can conclude that AUSM scheme is more efficient than the Roe scheme without showing excessive numerical dissipation. We can also state that the fifth-order WENO reconstruction is optimal one since there is no significant difference in accuracy between the fifth-order and seventh-order reconstructions.

5. Conclusions

Present study investigates the performance of six Riemann flux formulas for high-order reconstruction schemes. The third-, fifth-, and seventh-order weighted essential non-oscillatory (WENO) schemes are used as joint solvers with the idea of adaptive stencils to automatically achieve high order accuracy. In this framework, reconstructed left and right states for each cell are determined by using the WENO reconstruction procedures and used to calculate fluxes at cell edges. Then the Riemann solver is used to determine the flux from the reconstructed left and right states at the cell boundaries. Six state-of-the-art Riemann flux solvers are implemented in the current work, including Rusanov scheme, Roe scheme, Harten–Lax–Van Leer (HLL) scheme, first-order centered (FORCE) scheme, advection upstream splitting method (AUSM), and Marquina scheme. A systematic comparison and evaluation of these joint solvers are presented for solving the two-dimensional Kelvin–Helmholtz instability problem governed by Euler equations of gas dynamics.

The Kelvin–Helmholtz instability problem on a periodic two dimensional box is a challengingly appropriate benchmark test for evaluating ability to evolve a linear perturbation into a transition to nonlinear hydrodynamic two-dimensional turbulence. In fact, to be able to compare the dissipative and resolving properties of the joint numerical solvers more precisely we restrict ourselves to periodic boundary conditions and a uniform Cartesian grid. Consequently, we eliminate errors coming from the mesh non-uniformities and inconsistent boundary schemes. Initially, a single mode perturbation is used for our evaluations. Time evolution process shows that the small-scale vortices formed from the Kelvin–Helmholtz mechanism slowly merge together with time since both energy and enstrophy are inviscid invariants in the two-dimensional system.

According to the KLB theory of two-dimensional turbulence this system has an inertial subrange in the energy spectrum that is proportional to k^{-3} in the inviscid limit. The modular development of the joints solvers in this study provides an ease in evaluating the performance of high-order accurate WENO reconstruction schemes and different types of Riemann flux solvers. Based on a comprehensive assessment of the solutions obtained with all joint solvers on various resolutions, we showed that the energy spectrum in the inertial range flattens towards the classical k^{-3} scaling limit as the order of the reconstruction scheme increases due to lower numerical dissipation, in agreement with the KBL theory of two-dimensional turbulence. It is shown that the dissipative features of solvers affects eddy resolving properties and turbulence statistics. Order of reconstruction scheme becomes increasingly

important for coarsening mesh. We also demonstrate the AUSM methodology in computing Riemann fluxes at cell boundaries provides solutions with smaller numerical dissipation in all cases. We found that Roe solver agrees with theoretical energy spectrum with a marginal dissipation without showing a pile-up phenomenon even for underresolved simulations.

References

- [1] Lax PD. Weak solutions of nonlinear hyperbolic equations and their numerical computation. *Commun Pure Appl Math* 1954;7(1):159–93.
- [2] Godunov SK. A difference method for numerical calculation of discontinuous solutions of the equations of hydrodynamics. *Matematicheskii Sbornik* 1959;89(3):271–306.
- [3] Roe PL. Approximate Riemann solvers, parameter vectors, and difference schemes. *J Comput Phys* 1981;43(2):357–72.
- [4] Harten A. High resolution schemes for hyperbolic conservation laws. *J Comput Phys* 1983;49(3):357–93.
- [5] Sweby PK. High resolution schemes using flux limiters for hyperbolic conservation laws. *SIAM J Numer Anal* 1984;21(5):995–1011.
- [6] Anderson WK, Thomas JL, Van Leer B. Comparison of finite volume flux vector splittings for the Euler equations. *AIAA J* 1986;24(9):1453–60.
- [7] Harten A, Osher S, Engquist B, Chakravarthy SR. Some results on uniformly high-order accurate essentially nonoscillatory schemes. *Appl Numer Math* 1986;2(3):347–77.
- [8] Yee HC. Construction of explicit and implicit symmetric TVD schemes and their applications. *J Comput Phys* 1987;68(1):151–79.
- [9] Harten A, Engquist B, Osher S, Chakravarthy SR. Uniformly high order accurate essentially non-oscillatory schemes, III. *J Comput Phys* 1987;71(2):231–303.
- [10] Lax PD, Liu XD. Solution of two-dimensional Riemann problems of gas dynamics by positive schemes. *SIAM J Sci Comput* 1998;19(2):319–40.
- [11] Kurganov A, Tadmor E. New high-resolution central schemes for nonlinear conservation laws and convection-diffusion equations. *J Comput Phys* 2000;160(1):241–82.
- [12] Fjordholm US, Mishra S, Tadmor E. Arbitrarily high-order accurate entropy stable essentially nonoscillatory schemes for systems of conservation laws. *SIAM J Numer Anal* 2012;50(2):544–73.
- [13] Toro EF. Riemann solvers and numerical methods for fluid dynamics: a practical introduction. Springer; 2009.
- [14] Bertschinger E. Simulations of structure formation in the universe. *Ann Rev Astron Astrophys* 1998;36(1):599–654.
- [15] Lee TK, Zhong X. Spurious numerical oscillations in simulation of supersonic flows using shock-capturing schemes. *AIAA J* 1999;37(3):313–9.
- [16] Vos JB, Rizzi A, Darraqc D, Hirschel EH. Navier–Stokes solvers in European aircraft design. *Prog Aerosp Sci* 2002;38(8):601–97.
- [17] Ekaterinaris JA. High-order accurate, low numerical diffusion methods for aerodynamics. *Prog Aerosp Sci* 2005;41(3):192–300.
- [18] Tam CK, Webb JC. Dispersion-relation-preserving finite difference schemes for computational acoustics. *J Comput Phys* 1993;107(2):262–81.
- [19] Rajpoot MK, Sengupta TK, Dutt PK. Optimal time advancing dispersion relation preserving schemes. *J Comput Phys* 2010;229(10):3623–51.
- [20] Sengupta TK, Rajpoot MK, Saurabh S, Vijay V. Analysis of anisotropy of numerical wave solutions by high accuracy finite difference methods. *J Comput Phys* 2011;230(1):27–60.
- [21] Wang ZJ, Fidkowski K, Abgrall R, Bassi F, Caraeni D, Cary A, et al. High-order CFD methods: current status and perspective. *Int J Numer Meth Fluids* 2013;72(8):811–45.
- [22] Wang ZJ. High-order methods for the Euler and Navier–Stokes equations on unstructured grids. *Prog Aerosp Sci* 2007;43(1):1–41.
- [23] Shu CW. High order weighted essentially nonoscillatory schemes for convection dominated problems. *SIAM Rev* 2009;51(1):82–126.
- [24] Pirozzoli S. Numerical methods for high-speed flows. *Annu Rev Fluid Mech* 2011;43:163–94.
- [25] Sengupta TK. High accuracy computing methods: fluid flows and wave phenomena. Cambridge University Press; 2013.
- [26] Garnier E, Mossi M, Sagaut P, Comte P, Deville M. On the use of shock-capturing schemes for large-eddy simulation. *J Comput Phys* 1999;153(2):273–311.
- [27] Tenaud C, Garnier E, Sagaut P. Evaluation of some high-order shock capturing schemes for direct numerical simulation of unsteady two-dimensional free flows. *Int J Numer Meth Fluids* 2000;33(2):249–78.
- [28] Liska R, Wendroff B. Comparison of several difference schemes on 1D and 2D test problems for the Euler equations. *SIAM J Sci Comput* 2003;25(3):995–1017.
- [29] Greenough JA, Rider W. A quantitative comparison of numerical methods for the compressible Euler equations: fifth-order WENO and piecewise-linear Godunov. *J Comput Phys* 2004;196(1):259–81.
- [30] Kurganov A, Lin CT. On the reduction of numerical dissipation in central-upwind schemes. *Commun Comput Phys* 2007;2(1):141–63.
- [31] Thornber B, Mosedale A, Drikakis D. On the implicit large eddy simulations of homogeneous decaying turbulence. *J Comput Phys* 2007;226(2):1902–29.
- [32] Klingenberg C, Schmidt W, Waagan K. Numerical comparison of Riemann solvers for astrophysical hydrodynamics. *J Comput Phys* 2007;227(1):12–35.

- [33] Johnsen E, Larsson J, Bhagatwala AV, Cabot WH, Moin P, Olson BJ, et al. Assessment of high-resolution methods for numerical simulations of compressible turbulence with shock waves. *J Comput Phys* 2010; 229(4):1213–37.
- [34] Gao J, Li X, Wang Q. Effect of riemann flux solver on the accuracy of spectral difference method for CAA problems. *J Acoust Soc Am* 2012;131(4):3430.
- [35] Montecinos G, Castro CE, Dumbser M, Toro EF. Comparison of solvers for the generalized riemann problem for hyperbolic systems with source terms. *J Comput Phys* 2012;231(19):6472–94.
- [36] San O, Kara K. Numerical assessments of high-order accurate shock capturing schemes: Kelvin-Helmholtz type vortical structures in high-resolutions. *Comput Fluids* 2014;89:254–76.
- [37] Garnier E, Sagaut P, Deville M. Large eddy simulation of shock/homogeneous turbulence interaction. *Comput Fluids* 2002;31(2):245–68.
- [38] Garnier E, Sagaut P, Deville M. Large eddy simulation of shock/boundary-layer interaction. *AIAA J* 2002;40(10):1935–44.
- [39] Garnier E, Sagaut P, Deville M. A class of explicit ENO filters with application to unsteady flows. *J Comput Phys* 2001;170(1):184–204.
- [40] Liu XD, Osher S, Chan T. Weighted essentially non-oscillatory schemes. *J Comput Phys* 1994;115(1):200–12.
- [41] Jiang GS, Shu CW. Efficient implementation of weighted ENO schemes. *J Comput Phys* 1996;126:202–28.
- [42] Titarev VA, Toro EF. Finite-volume WENO schemes for three-dimensional conservation laws. *J Comput Phys* 2004;201(1):238–60.
- [43] Titarev VA, Toro EF. WENO schemes based on upwind and centred TVD fluxes. *Comput Fluids* 2005;34(6):705–20.
- [44] Ha Y, Ho Kim C, Ju Lee Y, Yoon J. An improved weighted essentially non-oscillatory scheme with a new smoothness indicator. *J Comput Phys* 2013;232(1):68–86.
- [45] Feng H, Huang C, Wang R. An improved mapped weighted essentially non-oscillatory scheme. *Appl Math Comput* 2014;232:453–68.
- [46] Fan P, Shen Y, Tian B, Yang C. A new smoothness indicator for improving the weighted essentially non-oscillatory scheme. *J Comput Phys* 2014;269:329–54.
- [47] Shen Y, Zha G. Improvement of weighted essentially non-oscillatory schemes near discontinuities. *Comput Fluids* 2014;96:254–76.
- [48] Kraichnan RH. Inertial ranges in two-dimensional turbulence. *Phys Fluids* 1967;10:1417–23.
- [49] Batchelor GK. Computation of the energy spectrum in homogeneous two-dimensional turbulence. *Phys Fluids* 1969;12:233–9.
- [50] Leith CE. Atmospheric predictability and two-dimensional turbulence. *J Atmos Sci* 1971;28(2):145–61.
- [51] Danilov SD, Gurarie D. Quasi-two-dimensional turbulence. *Phys Usp* 2000;43(9):863–900.
- [52] Tabeling P. Two-dimensional turbulence: a physicist approach. *Phys Rep* 2002;362(1):1–62.
- [53] Kellay H, Goldberg WI. Two-dimensional turbulence: a review of some recent experiments. *Rep Prog Phys* 2002;65(5):845–94.
- [54] Clercx HJH, van Heijst GJF. Two-dimensional Navier-Stokes turbulence in bounded domains. *Appl Mech Rev* 2009;62(2):020802.
- [55] Boffetta G, Ecke RE. Two-dimensional turbulence. *Annu Rev Fluid Mech* 2012;44:427–51.
- [56] Shu CW, Osher S. Efficient implementation of essentially non-oscillatory shock-capturing schemes. *J Comput Phys* 1988;77(2):439–71.
- [57] Gottlieb S, Shu CW. Total variation diminishing Runge-Kutta schemes. *Math Comput* 1998;67(221):73–85.
- [58] Gottlieb S, Shu CW, Tadmor E. Strong stability-preserving high-order time discretization methods. *SIAM Rev* 2001;43(1):89–112.
- [59] Borges R, Carmona M, Costa B, Don WS. An improved weighted essentially non-oscillatory scheme for hyperbolic conservation laws. *J Comput Phys* 2008;227(6):3191–211.
- [60] Hu XY, Wang Q, Adams NA. An adaptive central-upwind weighted essentially non-oscillatory scheme. *J Comput Phys* 2010;229(23):8952–65.
- [61] Kara K, Balakumar P, Kandil OA. Effects of nose bluntness on hypersonic boundary-layer receptivity and stability over cones. *AIAA J* 2011;49(12):2593–606.
- [62] Feng H, Hu F, Wang R. A new mapped weighted essentially non-oscillatory scheme. *J Sci Comput* 2012;51(2):449–73.
- [63] Aràndiga F, Baeza A, Belda A, Mulet P. Analysis of WENO schemes for full and global accuracy. *SIAM J Numer Anal* 2011;49(2):893–915.
- [64] Balsara DS, Shu CW. Monotonicity preserving weighted essentially non-oscillatory schemes with increasingly high order of accuracy. *J Comput Phys* 2000;160(2):405–52.
- [65] Rusanov VV. Calculation of intersection of non-steady shock waves with obstacles. *USSR Comput Math Math Phys* 1961;1:267–79.
- [66] LeVeque RJ. Finite volume methods for hyperbolic problems. Cambridge University Press; 2002.
- [67] Harten A, Lax PD, Van Leer B. On upstream differencing and Godunov-type schemes for hyperbolic conservation laws. *SIAM Rev* 1983;25(1):35–61.
- [68] Davis SF. Simplified second-order Godunov-type methods. *SIAM J Sci Stat Comput* 1988;9(3):445–73.
- [69] Trangenstein JA. Numerical solution of hyperbolic partial differential equations. Cambridge University Press; 2009.
- [70] Toro EF, Hidalgo A, Dumbser M. FORCE schemes on unstructured meshes I: conservative hyperbolic systems. *J Comput Phys* 2009;228(9):3368–89.
- [71] Stecca G, Saviglia A, Toro EF. Upwind-biased FORCE schemes with applications to free-surface shallow flows. *J Comput Phys* 2010;229(18):6362–80.
- [72] Liou MS, Steffen Jr CJ. A new flux splitting scheme. *J Comput Phys* 1993;107(1):23–39.
- [73] Liou MS. A sequel to AUSM: AUSM+. *J Comput Phys* 1996;129(2):364–82.
- [74] Wada Y, Liou MS. An accurate and robust flux splitting scheme for shock and contact discontinuities. *SIAM J Sci Comput* 1997;18(3):633–57.
- [75] Edwards JR, Liou MS. Low-diffusion flux-splitting methods for flows at all speeds. *AIAA J* 1998;36(9):1610–7.
- [76] Hong Kim K, Ho Lee J, Hyun Rho O. An improvement of AUSM schemes by introducing the pressure-based weight functions. *Comput Fluids* 1998;27(3):311–46.
- [77] Kim KH, Kim C, Rho OH. Methods for the accurate computations of hypersonic flows: I. AUSMPW+ scheme. *J Comput Phys* 2001;174(1):38–80.
- [78] Liou MS. A sequel to AUSM, Part II: AUSM-up for all speeds. *J Comput Phys* 2006;214(1):137–70.
- [79] Donat R, Marquina A. Capturing shock reflections: an improved flux formula. *J Comput Phys* 1996;125(1):42–58.
- [80] Donat R, Font JA, Ibáñez JM, Marquina A. A flux-split algorithm applied to relativistic flows. *J Comput Phys* 1998;146(1):58–81.
- [81] Chandrasekhar S. Hydrodynamic and hydromagnetic stability. Courier Dover Publications; 1961.
- [82] Frank A, Jones TW, Ryu D, Gaalaas JB. The magnetohydrodynamic Kelvin-Helmholtz instability: a two-dimensional numerical study. *Astrophys J* 1996;460:777–93.
- [83] San O, Staples AE. High-order methods for decaying two-dimensional homogeneous isotropic turbulence. *Comput Fluids* 2012;63:105–27.
- [84] San O, Staples AE. Stationary two-dimensional turbulence statistics using a Markovian forcing scheme. *Comput Fluids* 2014;71:1–18.
- [85] Stone JM, Gardiner TA, Teuben P, Hawley JF, Simon JB. Athena: a new code for astrophysical MHD. *Astrophys J Suppl Ser* 2008;178(1):137–77.